U. S. Naval Research Laboratory
Washington, DC 20375-5320

NRL/8230/FR--2022/1

TEPCE: A Tethered Electrodynamic Propulsion CubeSat Experiment

Shannon Coffey
Cameron Crippa
Systems Integration Branch
Spacecraft Engineering Division

Gil Dutchover
Matthew D. Brunner
Zachary Sibert
Scott Kindl
Dynamics and Control Systems Branch
Spacecraft Engineering Division

Ivan Galysh
Advanced Space PNT Branch
Space Systems Development Division

C. Lon Enloe
Charged Particle Physics
Plasma Physics Division

Joe Carroll
Tether Applications, Inc.

February 28, 2022

REPORT DOCUMENTATION PAGE

PLEASE DO NOT RETURN YOUR FORM TO THE ABOVE ORGANIZATION

1. REPORT DATE	2. REPORT TYPE	3. DATES COVERED	
02-28-2022	NRL Formal Report	START DATE 2010	END DATE 2020

4. TITLE AND SUBTITLE
TEPCE: A Tethered Electrodynamic Propulsion CubeSat Experiment

5a. CONTRACT NUMBER	5b. GRANT NUMBER	5c. PROGRAM ELEMENT NUMBER
5d. PROJECT NUMBER	**5e. TASK NUMBER**	**5f. WORK UNIT NUMBER** 6115

6. AUTHOR(S)
Shannon Coffey, Cameron Crippa, Gil Dutchover, Matthew D. Brunner, Zachary Sibert, Scott Kindl, C. Lon Enloe, Joe Carroll, Eugene Levin

7. PERFORMING ORGANIZATION / AFFILIATION NAME(S) AND ADDRESS(ES)
Naval Research Laboratory
4555 Overlook Avenue, SW
Washington, DC 20375-5320

8. PERFORMING ORGANIZATION REPORT NUMBER
NRL/8230/FR--2022/1

9. SPONSORING / MONITORING AGENCY NAME(S) AND ADDRESS(ES)	10. SPONSOR / MONITOR'S ACRONYM(S)	11. SPONSOR / MONITOR'S REPORT NUMBER(S)
Office of Naval Research One Liberty Center 875 N. Randolph Street, Suite 1425 Arlington, VA 22203-1995	ONR	

12. DISTRIBUTION / AVAILABILITY STATEMENT
DISTRIBUTION STATEMENT A. Approved for public release: Distribution unlimited.

13. SUPPLEMENTAL NOTES

14. ABSTRACT
TEPCE was a 3U Cubesat that was developed to explore the feasibility of using electrodynamic propulsion for spacecraft. Propulsion is generated by conducting an electric current along a long wire, called a tether, that connects two spacecraft end-masses. As the spacecraft moves along its orbital path the Earth's magnetic field induces a Lorentz force between the magnetic field and the electrons in the tether which results in thrust for the spacecraft. It requires no chemical or other traditional fuel source. TEPCE was one of the first self contained electrodynamic propulsion spacecraft.

15. SUBJECT TERMS

16. SECURITY CLASSIFICATION OF:			17. LIMITATION OF ABSTRACT	18. NUMBER OF PAGES
a. REPORT UNCLASSIFIED	b. ABSTRACT UNCLASSIFIED	c. THIS PAGE UNCLASSIFIED	None	45

19a. NAME OF RESPONSIBLE PERSON	19b. PHONE NUMBER *(Include area code)*
Shannon Coffey, Ph.D.	703-808-6798

This page intentionally left blank

CONTENTS

FIGURES

This page intentionally left blank

EXECUTIVE SUMMARY

TEPCE was a 3U CubeSat that was developed to explore the feasibility of using electrodynamic propulsion for spacecraft. Propulsion is generated by conducting an electric current along a long wire, called a tether, that connects two spacecraft end-masses. As the spacecraft moves along its orbital path, the Earth‘s magnetic field induces a Lorentz force between the magnetic field and the electrons in the tether that results in thrust for the spacecraft. It requires no chemical or other traditional fuel source. TEPCE was one of the first self-contained electrodynamic propulsion spacecraft. TEPCE was launched on a SpaceX Falcon Heavy rocket on June 25, 2019. It was a successful spacecraft that demonstrated mechanical and electrical systems that can enable a spacecraft to maneuver using electrodynamic principles.

This page intentionally left blank

TEPCE: A TETHERED ELECTRODYNAMIC PROPULSION CUBESAT EXPERIMENT

1. INTRODUCTION

TEPCE was a 3U CubeSat created by the Naval Research Laboratory to test electrodynamic propulsion. This document describes the design, which was patented in 2015[1], and the flight operations for TEPCE. It was launched into a 830×300 km, 28.5^{o} inclined orbit aboard the SpaceX Falcon Heavy booster on June 25, 2019. As launched, TEPCE was a 3U CubeSat. It consisted of two end-masses that are nearly identical 1.5U CubeSats and a center module consisting of a stacer separation spring and a spool of tether. An illustration of how TEPCE might have appeared in space is provided in Fig. 1. The end-masses were separated on November 16, 2019.

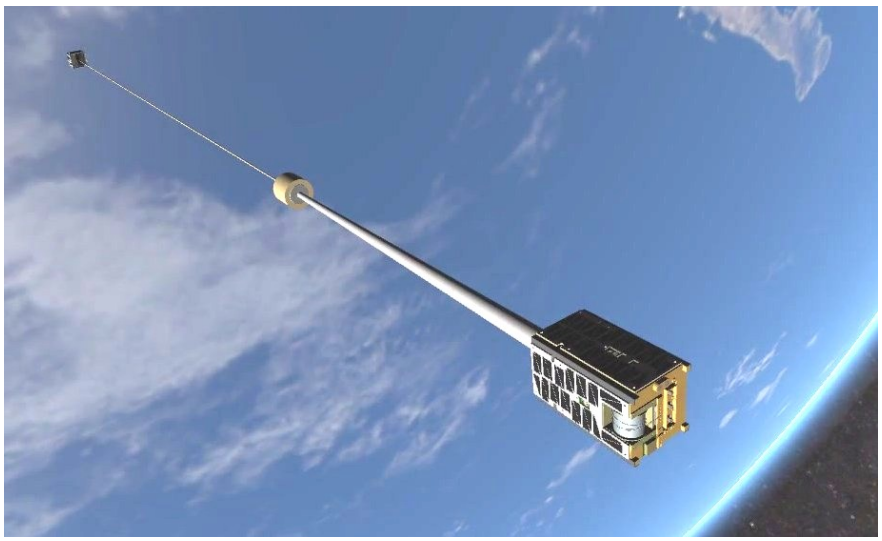

Fig. 1—3D Rendering of Tether Deployment

Propulsion for TEPCE was based on a physics principle called electrodynamics, which involves conducting an electric current along a tether between two end-masses. The electrodynamic components in TEPCE start with a 5-meter metal collector tape on each end-mass that collect electrons from the earth's plasma. Each end-mass also has two tungsten filaments that emit electrons back to the plasma. The collector tapes, tether, and emitter filaments can be connected electrically to allow electrons to flow from the collector tape, across the tether, to the emitter filaments. The plasma acts as the source of electrons, much like a battery in a DC circuit. Figure 2 illustrates the physics principle.

The force produced by the electrodynamics is called a Lorentz force. The force vector is given by

$$\boldsymbol{F} = i\boldsymbol{L} \times \boldsymbol{B},$$

Manuscript approved February 28, 2022.

where i is the current flowing through the tether, $\boldsymbol{L}$ is the vector along the tether and $\boldsymbol{B}$ is the magnetic field vector. The longer the tether and the greater the current, the stronger the force on TEPCE. Electrons are collected from the plasma on a collector tape at one end of the system or on the tether and are conducted along the tether to an emitter filament on an opposing end-mass, where the electrons are expelled into the plasma. Thus, the current circuit is closed through the Earth's plasma. The concept is illustrated in Fig. 2. TEPCE has emitter filaments on the outward-facing surface of both Ren and Stimpy. In the illustration of Fig. 2a, Ren is at the bottom, as is the Earth, so the electrical current is flowing towards the Earth. This results in thrust in the direction of the velocity vector, which would enable TEPCE to climb in altitude. TEPCE was built to emit electrons through Stimpy also, and in the configuration depicted in Fig. 2b, TEPCE could produce thrust against the velocity vector, inducing added drag on the vehicle. The plasma is both a sink and a source of electrons, much like a battery. Thus the plasma and TEPCE's electrodynamic circuitry acts like a closed circuit, with current flowing in one direction along the tether. TEPCE was designed as a 3U CubeSat. The crowded internal space of this 3U CubeSat made it extremely difficult to accommodate all the mechanical and electrical components. Volume constraints resulted in selection of a 1-km tether.

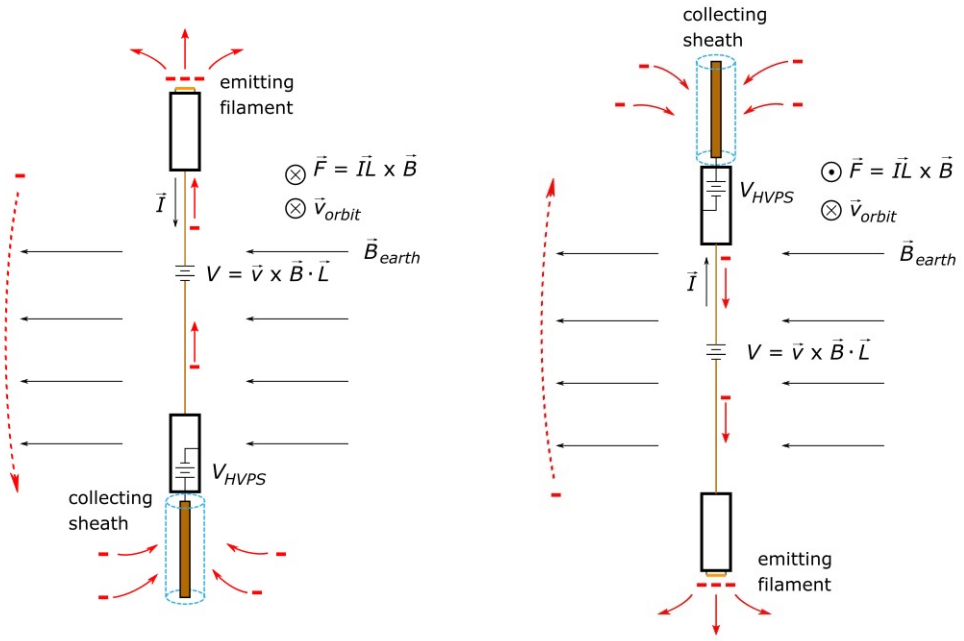

(a) Current Flow in Thrusting Mode

(b) Current Flow in Drag Mode

Fig. 2—Current Interaction with Plasma

During the mission, TEPCE only was able to emit electrons from REN, which was the nearest end-mass to the Earth. Effectively, this produced a drag on TEPCE from the electrodynamic thrusting.

2. DESCRIPTION OF TEPCE

The description of TEPCE begins with the two end-masses Ren and Stimpy. A picture of the completed TEPCE spacecraft is provided in the two images in Fig. 3. CAD drawings of the components of TEPCE are provided in Fig. 4.

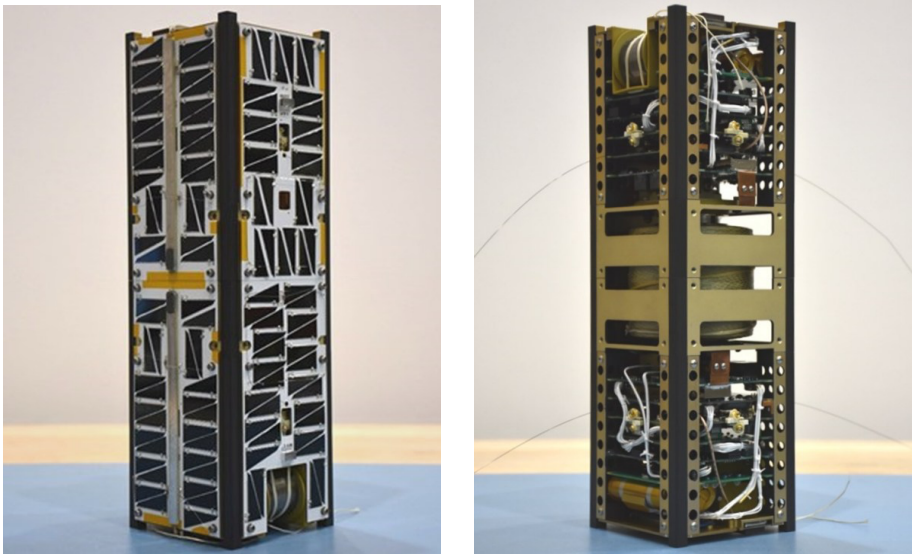

(a) TEPCE configured for flight (b) TEPCE with solar panels removed

Fig. 3—TEPCE

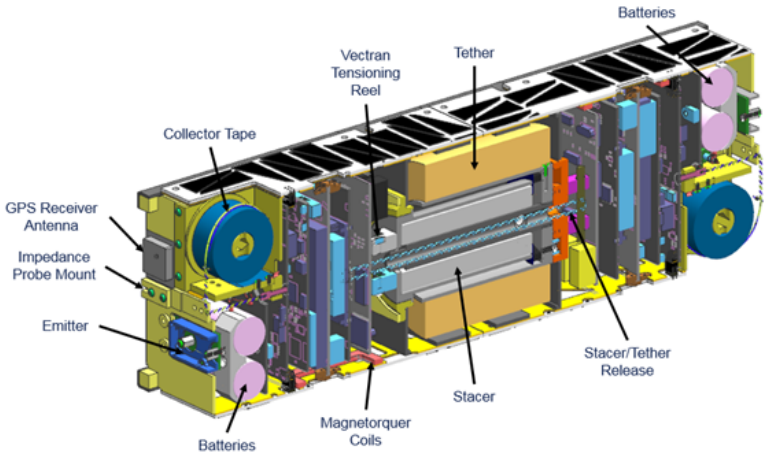

(a) CAD cutaway drawing of TEPCE

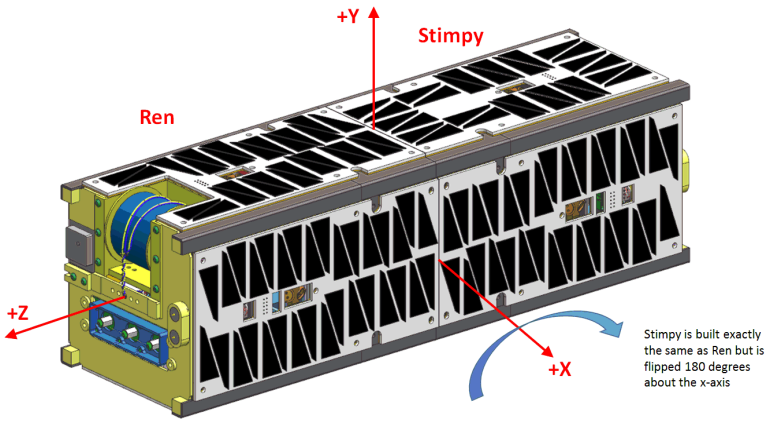

(b) TEPCE coordinate system

Fig. 4—TEPCE Layout

To produce the separation of the two end-masses, a stacer spring was used. It was fitted inside the tether winding that took up most of the "center cube" of the 3U CubeSat. A stacer looks like a wound-up clock spring, but deploys axially, into a rigid boom. The stacer exerted force against the two end-masses effectively "shot-putting" one end-mass away from the other, and also converting the stowed tether and the other end-mass into a long, rigid dumbbell. A 1.5-m dumbbell could reduce any prior rotation rate by a factor of 60, and also could create a large moment arm to align the winding with the deploying tether, even with very low deployment tension. This concept crystallized TEPCE's hardware design.

Externally, Ren and Stimpy were covered with body-mounted solar arrays on the four 15 cm x 10 cm x 10 cm sides. On the Z face of the end-masses are several electrodynamics components, as seen in Fig. 4b,.

The electron collectors (one on the Z face of each end-mass) consist of a 1 in x 0.010 in x 5 m rolled-up metal tape. Supplied by the Stanley Works Corporation, it is identical to a carpenter's tape without the numbers and painting. Considerable effort was invested to determine whether this collector tape would function properly after a long, sustained period in its stowed configuration.

The main concern with the collector tape was whether it would rust along its length between the windings, thus inhibiting its deployment. There was also concern with rust inhibiting its ability to attract electrons. It turned out that it was stowed for over five years before launch. It is believed both collector tapes deployed properly. However, due to communication problems with Stimpy, there was no way to determine the collector tape's contribution to the current flow. The plan was to bias the collector tape positively to attract electrons. On each end-mass were tungsten filaments whose job was to emit the electrons into the plasma. Since there were collector tapes on each end-mass and electron filaments on each end-mass, it was possible to conduct current in either direction along the tether. Because of communication problems with Stimpy, electron flow was established only in one direction, from Stimpy to Ren. As a result of being unable to command the collector tape circuitry on Stimpy, electrons were not able to be collected on the collector tape. Nonetheless, electrons were able to be collected along the tether and thus demonstrated the electrodynamic concept in this way.

The separation of the end-masses was accomplished by a single telescoping spring called a stacer that was anchored to Ren. The ball of tether was attached to the opposite end of the stacer nestled between the stacer and Stimpy. The two end-masses were held together with cords of Vectran. There were no hard bolts connecting the end-masses. The end-masses were merely tied together with Vectran cords. To release the end-masses, burn wires [2] consisting of resistor were used to burn through the arresting cords.

Deployment was initiated manually and occurred on November 16, 2019, at 01:47 a.m. EST during a pass over the Key West ground station. The stacer tie-downs were cut, the stacer pushed the end-bodies apart, and the tether began paying off the spool, as shown in Fig. 1.

3. TEPCE MECHANICAL STRUCTURE

The two 1.5U sub-CubeSats of TEPCE are called Ren and Stimpy, after the animated television series from the 1990s. This was a continuation of a tradition at the Naval Research Laboratory of naming the end-masses of tethered spacecraft after characters from television programs [3].

Ren and Stimpy (RS) are largely identical, with the exception of the spring and the tether, which will be described later.

3.1 Mechanical Description of Ren

The main structure of Ren consists of an end panel and a bulkhead separated by four rails that are tied together with four side panels. The emitter and collector assemblies are mounted to the end panel. The tether and tension mechanism assemblies are mounted to the bulkhead, as seen in Fig. 5.

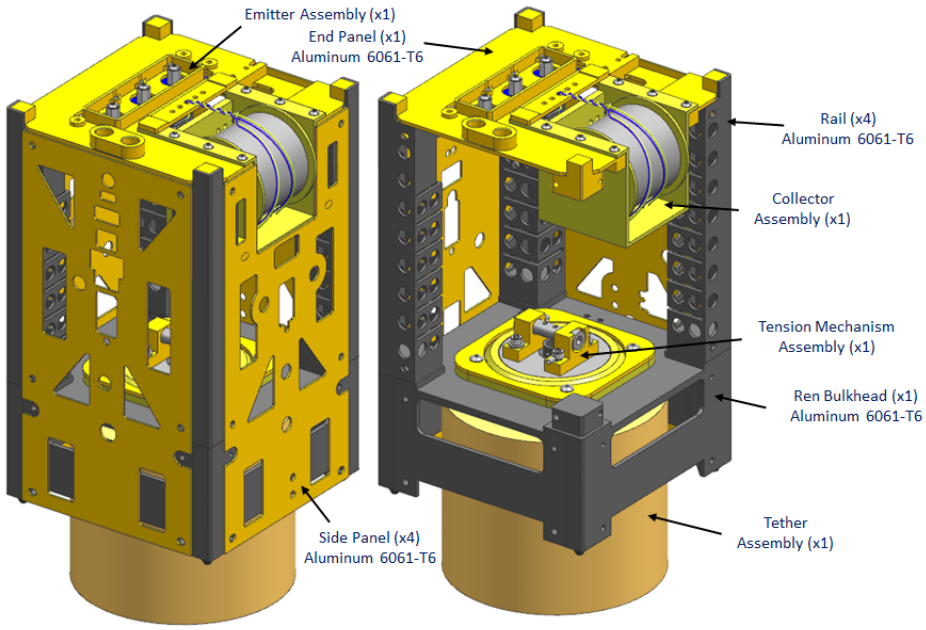

Fig. 5—Ren structural components and subassemblies

The end panel, side panels, rails and bulkhead are made of aluminum 6061-T6 and are chemical conversion coated, MIL-C-5541 class 3, and hard anodized with PTFE, MIL-A-8625 type 3 class 1. The chemical conversion coated areas create Ren's ground plane, while the hard anodized surfaces create a sliding interface between TEPCE and the PPOD and provide insulation where required.

The tension mechanism generates preload between Ren and Stimpy, constraining the stacer spring. The tension mechanism contains a modified shoulder bolt and a locking fastener, seen in Fig. 6. The function of the tension mechanism will be discussed in Section 3.3.

The emitter assembly comprises a G10 interface plate, an aluminum 6061-T6 emitter trough, and two thoriated tungsten emitter filaments. The G10 interface plate provides insulation between the vehicle chassis and the high-voltage emitter filaments, illustrated in Fig. 7.

The collector assembly, shown in Fig. 8, is made of a blued carbon steel collector, a Torlon 420 3L collector housing, and two burn wire release mechanisms [2]. The Torlon collector housing provides insulation between the vehicle chassis and the high-voltage collector. The collector is stowed using a twisted pair of 12-strand 200 denier Vectran cords. The Vectran is routed through the collector housing and around the collector, and is tied to a tension set screw. The collector is preloaded into the collector housing by adjusting the tension set screw. The collector is released by running current to either of the burn wire release mechanisms.

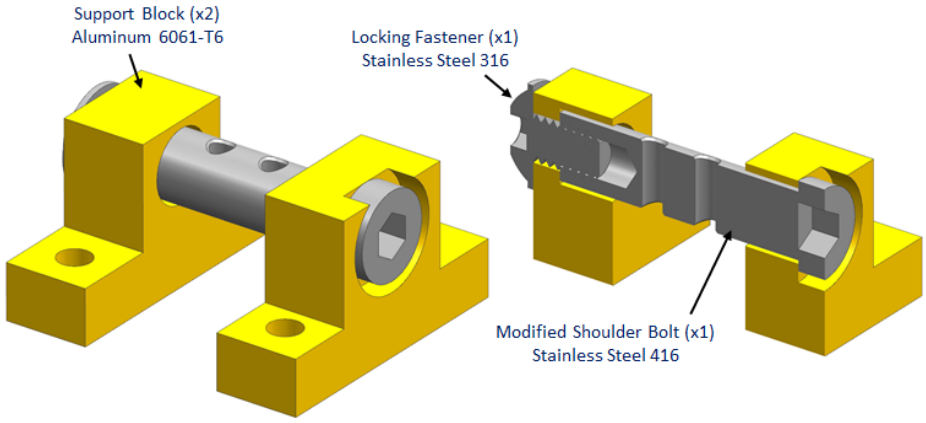

Fig. 6—Tension mechanism assembly

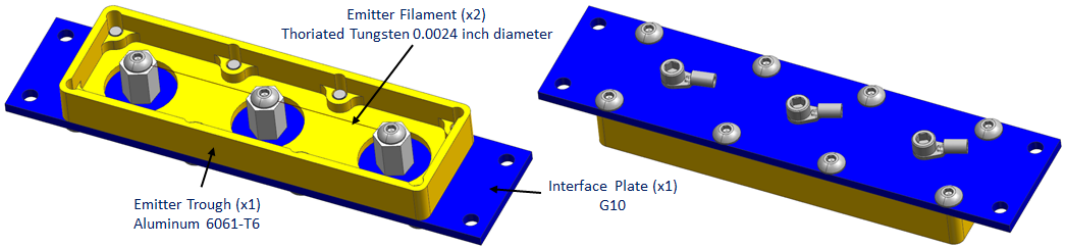

Fig. 7—Emitter assembly

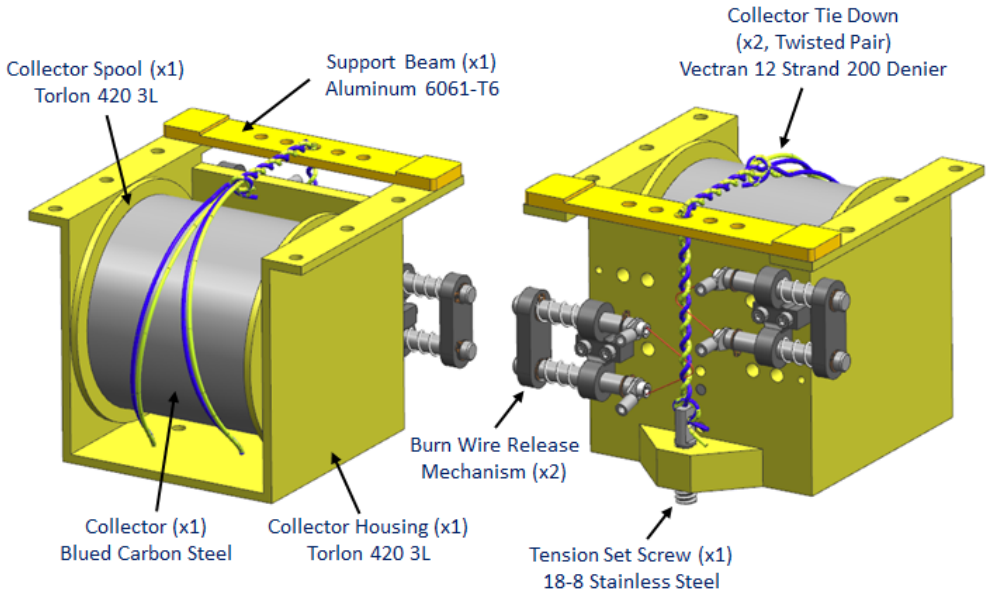

Fig. 8—Collector assembly

The burn wire release mechanism consists of two hard anodized aluminum 6061-T6 support saddles, two 18-8 stainless steel guide pins, and a 30 AWG Nichrome chromel C burn wire. The hard anodized support saddle isolates the mechanism from vehicle chassis. Current is supplied to the guide pins, heating up the burn wire. The burn wire melts through the Vectran tie-down. Two springs generate a compressive force between the support saddles. In the stowed position, tension in the tie-down reacts to this compressive force. As the burn wire melts through the tie-down, this compressive force is released, allowing the mechanism to fully stroke through the tie-down. The burn wire release mechanism is illustrated in Fig. 9.

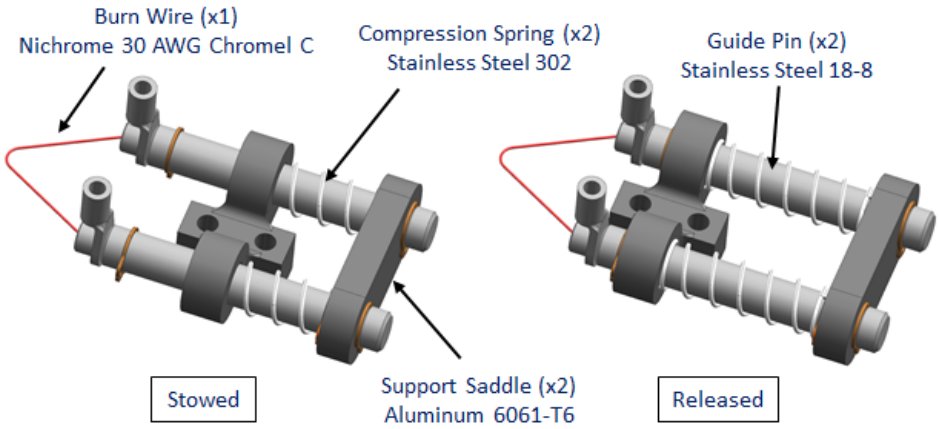

Fig. 9—Burn wire release mechanism

The tether assembly consists of an Elgiloy stacer spring, a Torlon 420 3L stacer interface, and a 9-strand 200 denier Kevlar and Aracon tether. The Torlon stacer interface provides insulation between the vehicle chassis and the high-voltage tether and stacer spring. The stacer spring provides 35 N of separation force between Ren and Stimpy and has a deployed length of 4 m, illustrated in Fig. 10.

3.2 Mechanical Description of Stimpy

The main structure of Stimpy consists of an end panel and a bulkhead separated by four rails and tied together with four side panels. The emitter and collector assemblies are mounted to the end panel and the tether interface is mounted to the bulkhead, shown in Fig. 11.

The stacer release assembly deploys the stacer spring, separating Ren and Stimpy. The stacer release assembly contains two burn wire release mechanisms and a support rod, seen in Fig. 12. The function of the stacer release assembly will be discussed in Section 3.3.

The Torlon 420 3L tether interface provides an end point for the tether. The Torlon insulates the high-voltage tether from the vehicle chassis.

3.3 Mechanical Description of Center Module

The center module, shown in Fig. 13, shares components from both Ren and Stimpy and is the separation interface of TEPCE. The center module comprises Ren‘s bulkhead, Stimpy‘s bulkhead, the tether assembly, the tension mechanism, and the tether release assembly.

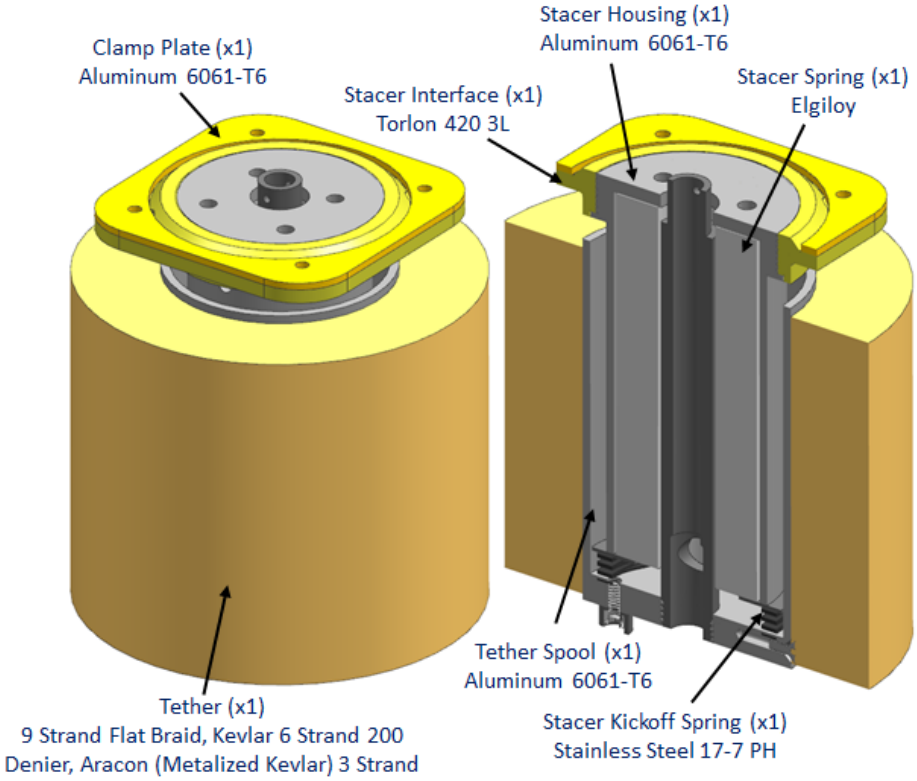

Fig. 10—Tether assembly

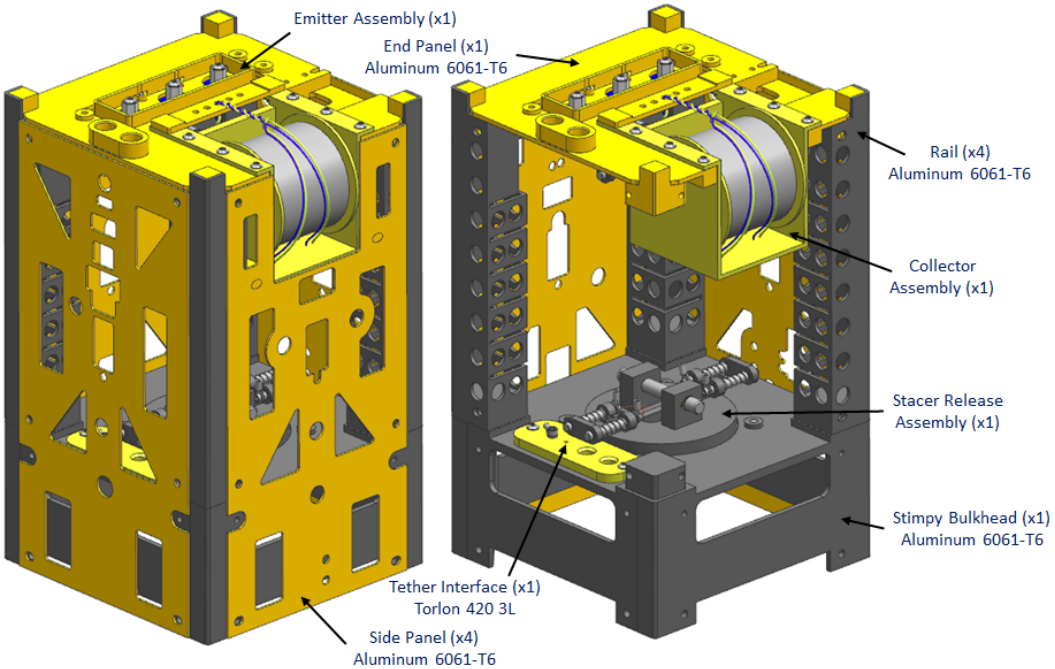

Fig. 11—Stimpy structural components and subassemblies

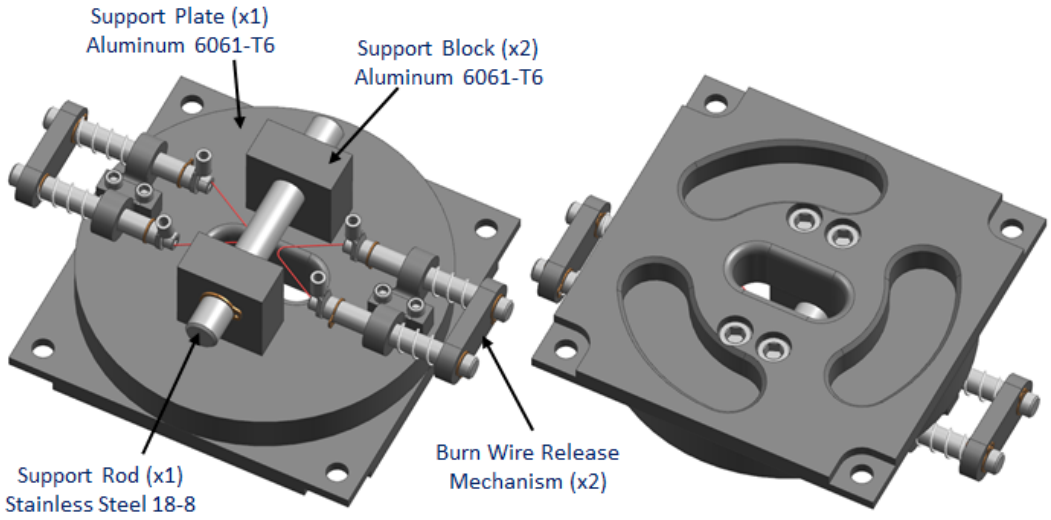

Fig. 12—Stacer release assembly

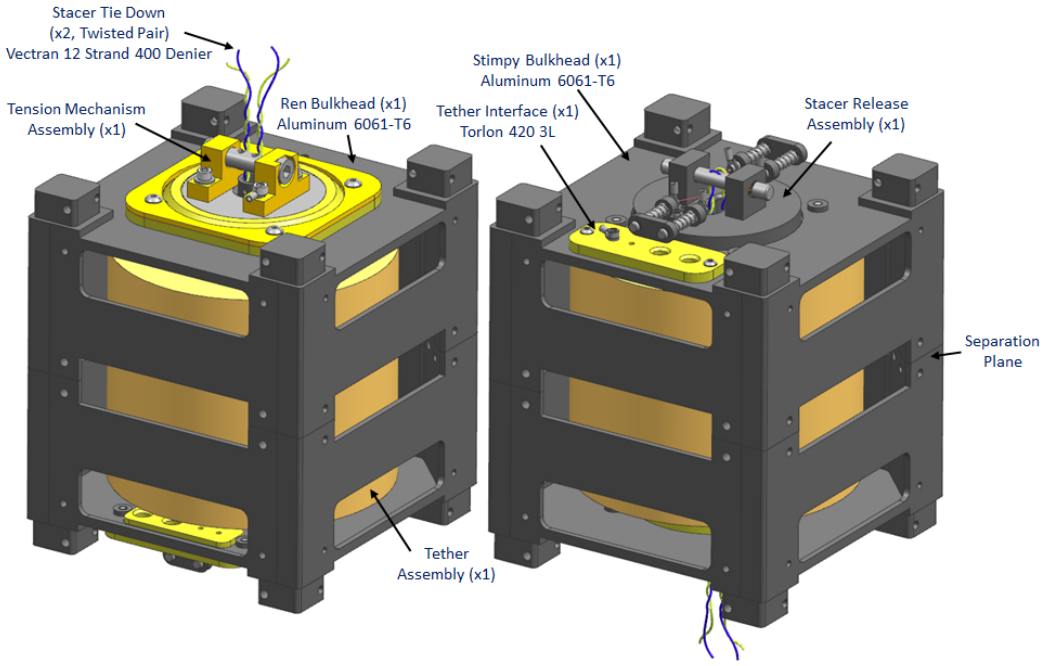

Fig. 13—TEPCE center module

The stacer spring is stowed in the center module using a twisted pair of 12-strand 400 denier Vectran cords. The Vectran is routed around the stacer release assembly support rod and through the center of the tether assembly, and is tied to the tension mechanism. The two bulkheads are preloaded against one another by applying torque to the tension mechanism‘s modified shoulder bolt. This torque generates tension in the Vectran and is held in place with the tension mechanism‘s locking fastener. The Vectran is routed so that the tension tightens the modified shoulder bolt into the locking fastener; see Figs. 6, 11, and 12.

The stacer spring is released, separating Ren and Stimpy, by supplying current to either of the burn wire release mechanisms in the stacer release assembly, seen in Fig. 12.

3.4 Tether Design, Winding and Testing

The design assumed a bare tether instead of an insulated tether because insulation would add stiffness and bulk, while the bare conductor could collect electrons that could emit from both end-masses simultaneously. Then, current could flow in opposite directions on each half of the tether, thus causing opposite distributed forces on each half. This could have let mission operations actively drive and dampen libration. While this design gave more experiment options, ultimately, those options were not able to be exercised during the mission. In operations, only the lower end-mass worked properly. Since current flow from the collector tape on the upper end-mass, Stimpy, could not be controlled, the tether was used as a remote electron collector.

To make the tether conductive, a metal-coated Kevlar fiber, Aracon, was used. The metal adds 40% to the volume of a 200 denier strand of 14 micron Kevlar fibers but adds 250% to its mass. The coating is nickel/copper/nickel. It has half the conductivity of bulk copper per added mass. Kevlar was also used for the non-conductive strands since Aracon might heat up enough in the sun to damage high-strength Spectra polyethylene fibers. A flat nine-strand braid was used to increase lifetime against impacts, but at the cost of higher aerodynamic drag, and hence shorter orbit life after tether deployment. Six 200 denier Kevlar strands plus three Aracon strands were used. The braid is 1.6 mm wide and 0.25 mm thick and has an average drag width of 1.1 mm. About 37% of the exposed area is metal. Electrical resistance is 1.6 ohms/m at 300K, and nearly scales linearly with absolute temperature. The deployable length is 1030 m. The tether weighs 420 grams, of which 230 grams is the Aracon metal coating. The completed tether winding is shown in Fig. 14.

Fig. 14—Completed tether winding

The tension of a vertical 1 km, 4 kg dumbbell in LEO is 3 - 4 mN. (The tether weighs 4 mN/m on the ground.) The 1993 PMG [4] test resulted in a large rebound after deployment from energy storage in a

weakly damped rotating wiggle. The TEPCE team decided to reduce the tether angular momentum caused by free endwise deployment by reversing the tether wind direction five times during the winding. Fig. 15a shows one of the reversals. Slow-motion video of deployment (with the tether falling under its own weight in air) showed that the winding and reversals paid out freely.

(a) Tether winding reversal

(b) Tether braking hooks

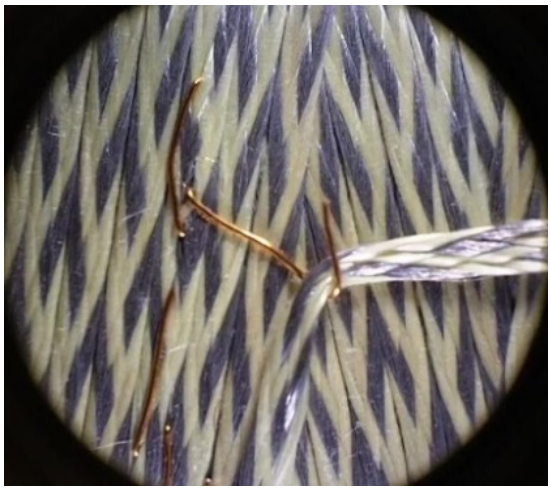

(c) Tether pulling on hooks

Fig. 15—Tether Winding Details

It was difficult to envision a reliable, yet sufficiently weak, adhesive brake, so brakes using bent pieces of 36 AWG magnet wire were inserted in the winding. The strategy was to stretch the tether and to cause fast payout at the end so as to dump energy into faster modes that can damp faster. As shown in Fig. 15, each wire was stitched through one turn, and then each end was wrapped around another turn. There were 64 hooks in the last 110 m, with changes in hook shape to ramp up the release force from 0.1 N to 0.5 N. The hook spacing was 1.7 m, except that each group of 16 hooks had an extra 0.85-m offset to ease counting accelerometer jerks and to determine how much tether paid out.

The 1030-m tether was wound on a 80-mm-long, 51-mm-diameter cup-like core that held the stacer spring. Figures 14 and 15 show the completed winding. The winding is 86 mm in diameter, and tapers in length 79 to 70 mm along the length.

3.5 Antenna Routing

Due to height restrictions in the P-Pod, no more than 6.5 mm was available above the rail surface for components. The antennas were 9 mil nitinol wires attached directly to the radio circuit board. Since nitinol cannot be soldered easily, the nitinol wire was crimped in a small connector pin. The pin then was soldered to the radio circuit board.

To secure the antenna, a 6-pound nylon cord or fishing line was tied to the end of the antenna. To provide a catch at the end of the antenna so the nylon cord does not slip, the tip of the antenna was flattened by using a hammer and an anvil as shown in Fig. 16. The antenna wire had to be struck with enough force to cause the wire to flatten. This was done experimentally by hand. Multiple antenna wires were flattened and the best ones were used.

Fig. 16—Flattened end of antenna

For routing the antenna to secure it for launch, the posts, shown in Fig. 17, consisted of cap head machine screws with custom-made spacers with a concave shape to trap the wire and the cord. The antenna was routed out of the solar panel to the top left post, then was looped to the right, down and left to the bottom post. Just to the right of the bottom post, was a resistor cutter. The nylon cord was wrapped over and then under the resistor to reduce the chance that the nylon would stick to the resistor upon release.

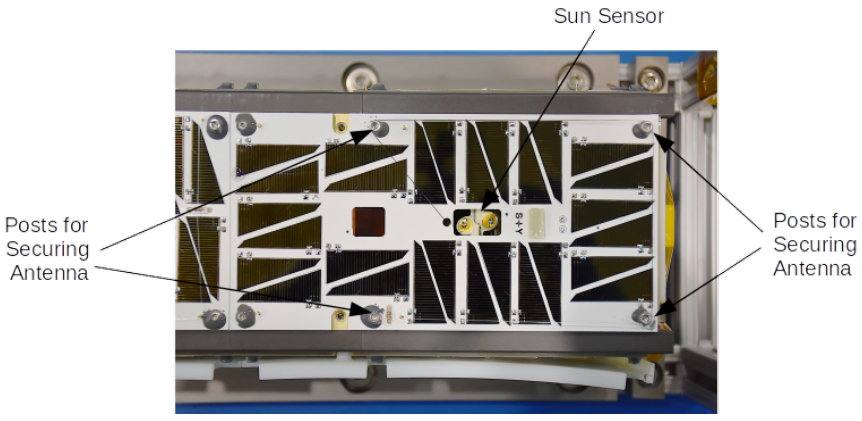

Fig. 17—Antenna routing on solar panel

4. ELECTRONICS DESCRIPTION OF TEPCE

The electronic cards are mounted to the rails, as seen in Fig. 18.

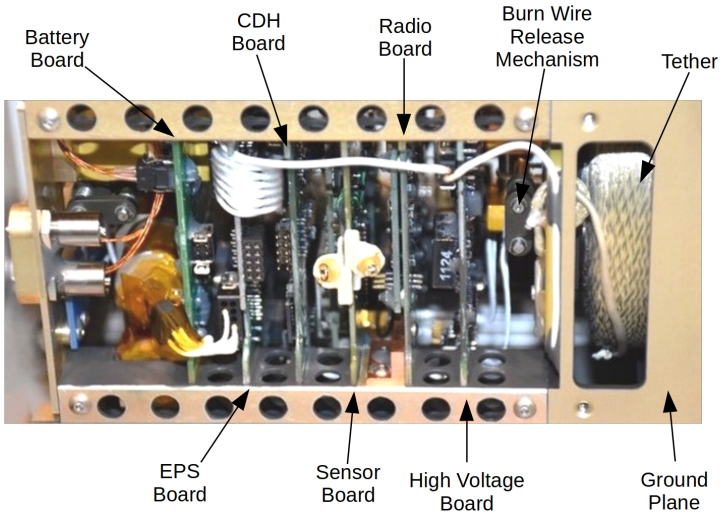

Fig. 18—TEPCE board stack, tether, collector tape, and filaments

Ren and Stimpy have identical electronics. The software operating the electronics is also identical, with only the identification parameters being unique in the software. Figure 19 shows the block diagram of the electronics and how they are interconnected.

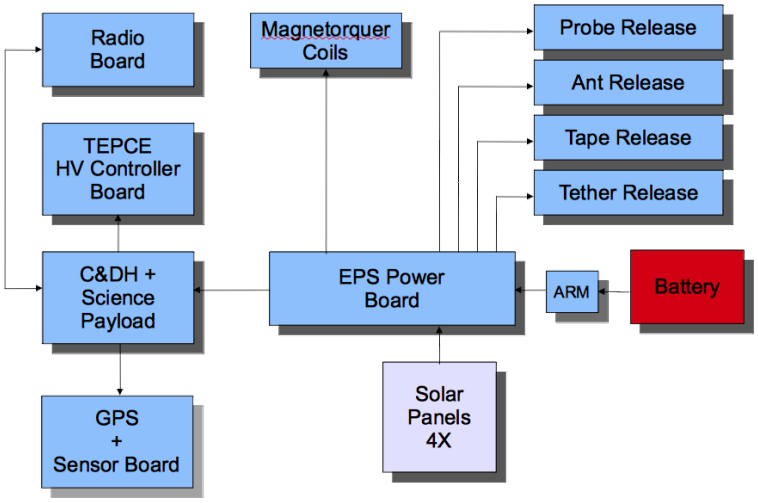

Fig. 19—End mass electronics block diagram

The electronics is a stack of six circuit boards. The stack of boards includes the battery board, the electrical power system (EPS) board, the computer data handling (CDH) board, the sensor board, the radio board and the high-voltage board. The boards are interconnected with harnesses.

4.1 Battery Board

The battery board, shown in Fig. 20, contains two 18650 lithium ion cells. LG brand cells were selected, as they were readily available in single-piece quantities, met the temperature range expected and were from a primary manufacturer and not from a secondary, rebranded source. The cells operated at an average of 3.6 volts and had capacity of 2600 mAH. They were able to provide up to 3.75 amperes of current; at most, 2 amperes were needed by the satellite.

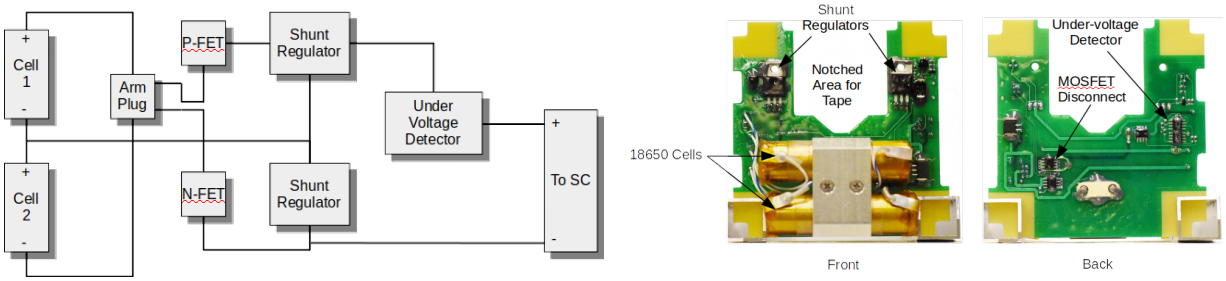

(a) Battery board block diagram (b) Battery board

Fig. 20—Battery board system

The circuitry on the battery board included shunt regulators for each cell that clamped the maximum voltage at 4.1 volts. An undervoltage detector circuit kept the cells from discharging below 6 volts. A large P-channel field-effect transistor, FET, was used to disconnect the battery circuit from the satellite if the voltage dropped below 6 volts. The FET included a protection diode that was used to allow solar power to charge the cells.

The battery board included the arm plug. The arm plug electrically disconnected the cells from all circuitry. A release switch also was connected to the battery board and was used to turn on the satellite when it was released from the PPOD. When the switch was released, a P-channel voltage controlled field effect transistor, MOSFET, and N-channel MOSFET were turned on, connecting the cells to the protection circuits and the satellite bus.

4.2 Electrical Power System (EPS)

The EPS board, shown in Fig. 21, had multiple functions. The main function was providing a 5-volt supply to the command data handler, the sensor, the radio and the high-voltage board. The 5-volt regulator was a DC-DC converter with 4 amperes capacity that was needed to handle the inrush current from the iProbe circuit.

A discrete watchdog timer was included on the EPS board. It used a capacitor charge circuit to trip a comparator that would turn power off to the satellite bus. An 8-ampere P-channel MOSFET was used as the switch. The CDH had to reset the watchdog timer within 6 seconds or power would be turned off for about 4 seconds, which allowed all capacitors to discharge and all circuits to be off. Any time the CDH crashed due to software error or radiation event, the watchdog timer power-cycled the whole satellite.

An eight-channel analog-to-digital converter (ADC) collected solar panel currents, battery current and battery voltage. The solar panels were connected directly to the EPS board on all four sides by directly

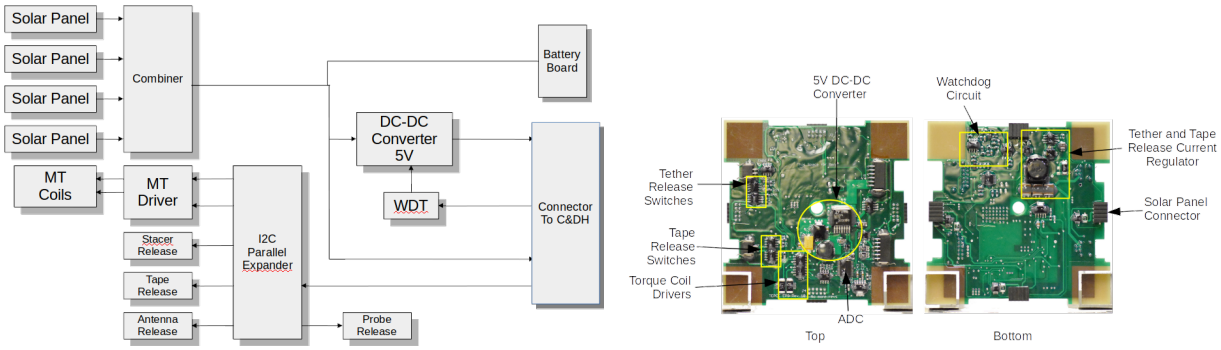

(a) Electrical power system block diagram

(b) Electrical power system board

Fig. 21—Electrical Power System

plugging using a board-to-board connector. Current sensor circuits were on the EPS board. The current-sensing circuitry indicated the direction of the battery current, which allowed the ground operator to know whether the battery was being charged and which solar panels provided power.

The EPS board included circuits for controlling the two magnetic torque coils using a bidirectional motor driver IC. This simple circuit turned the coils on and off and set the polarity. The current was set by the coil windings.

The EPS also controlled the cutters for deploying the antennas, the iProbe, the tether, and the collector tape using a constant-current circuit. The circuit provided a constant current independent of the harness impedance.

4.3 Solar Panels

The solar panels were circuit boards with up to eight strings of solar cells, each string containing four solar cells. The strings were combined on the solar panels through diodes. The solar cells were triangular triple-junction cells from Spectrolabs. Four cells in series provided the proper voltage to charge the battery, directly eliminating the need for a complex charger circuit. Each string could provide up to 28 ma at maximum power, with eight strings providing over 220 mA of current. The solar panels were built on four-layer circuit boards, which included a solid copper ground plane. The other layers were used for routing power and to allow the power routes to be spread across the panel to maximize the spread of the current flows to minimize torque caused by currents. The solar panel assembly included a 0.032- in-thick sheet of aluminum mounted to the back side of the solar panel circuit board with a sheet of kapton in between to eliminate the possibility of short circuits.

Each of the four solar panels was a unique design and included additional functions. The ARM panel, seen in Fig. 22, was so named because it was on the side with the arming plug access hole that provided access to the arming connector on the battery board. This side also included a debugging/programming connector located on the CDH board. A recharging connector located above the access areas allowed external recharging of the battery.

The GPS panel, seen in Fig. 23, included a cutout for a GPS antenna that wound up not being used. The panel included a 1/8-watt, 10-ohm resistor for melting a nylon cord to release one of the two antennas. The

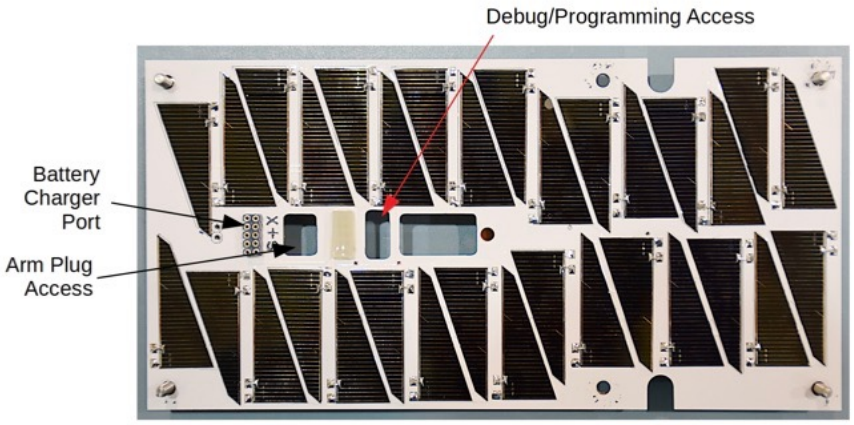

Fig. 22—ARM Panel

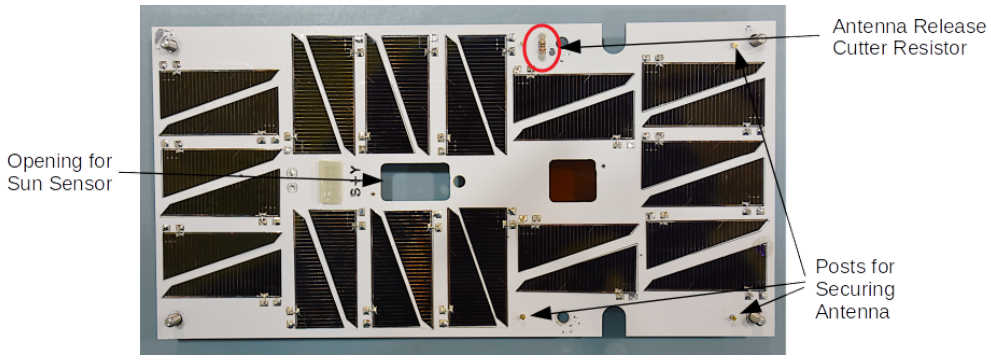

Fig. 23—GPS solar panel

resistor was powered at 5.5 volts for 10 seconds, which caused the resistor to overheat and to melt the nylon cord. Three printed circuit mounted test posts were placed on the solar panel to wrap the antenna and nylon cord to stow during launch.

The iProbe panel, seen in Fig. 24, included two 1/8-watt, 10-ohm resistors to cut the nylon cord holding down the iProbe probe. The resistors were powered by the same 5.5-volt source to melt the nylon cord. Due to the space taken by the probe, only seven strings of solar cells fit on the panel. The probe was positioned down the center of the panel, requiring the solar cells to be moved to the edge of the panel to avoid contact with the probe during launch and deployment. The panel had a hand-wound magnetorquer coil epoxied to the back side of the panel. The board-to-board connector to the EPS board provided the connection for the coil.

The NOTCH panel, seen in Fig. 25, had a large notch at the top for the collector tape to be released. It had only seven strings of solar cells due to the notch. It also had a 1/8-watt 10-ohm resistor to release the second antenna. The NOTCH panel had a magnetorquer coil epoxied to the back side and used the board-to-board connector to the EPS for the connection.

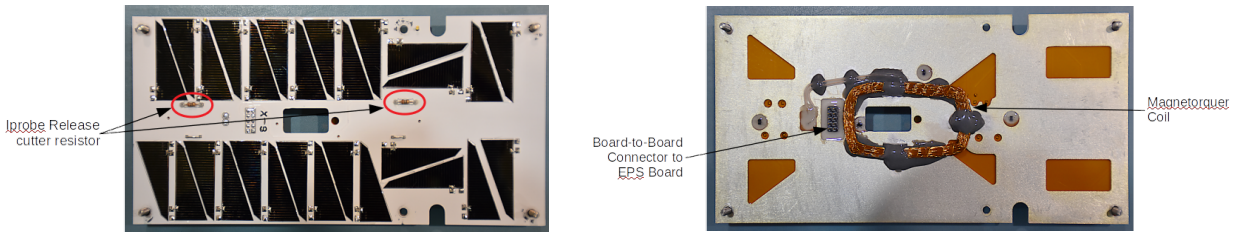

(a) iProbe panel top side (b) iProbe panel bottom side

Fig. 24—iProbe

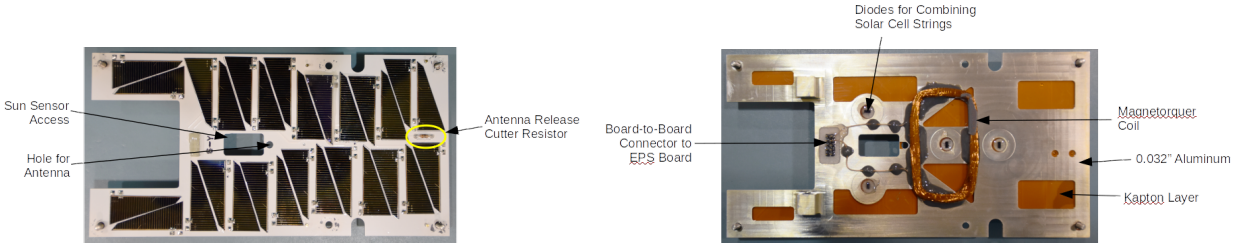

(a) Notch panel top side (b) Notch panel top side

Fig. 25—Notch panel

4.4 Command Data Handling Board (CDH)

The CDH board, seen in Fig. 26, used a STM32F103 ARM-based 32-bit microcontroller operating at 72 MHz. The microcontroller executed the flight software and controlled all functions. It had five asynchronous serial ports used to communicate with other processors in the satellite and provided a debugging and programming port. The I2C interface connected to the EPS board to control all of its circuits. Included on the CDH board was a real-time clock for maintaining satellite time, an EEPROM IC for holding state information if the CDH rebooted, P-channel MOSFETS for switching power to the GPS receiver, the sensor

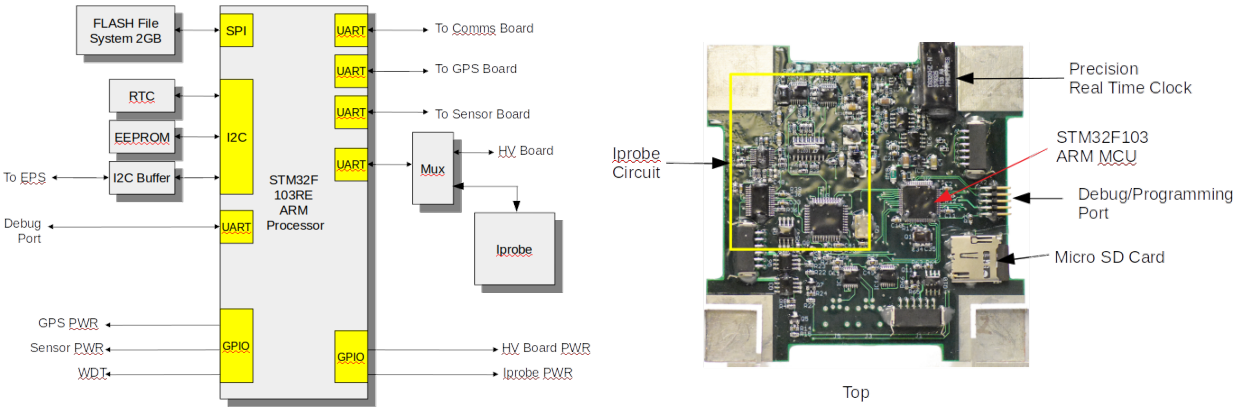

(a) CDH board diagram (b) CDH board

Fig. 26—Command data handling (CDH)

board, and the high-voltage board, and a 2 GB microSD card. The microSD card was chosen because large-size memory ICs were not readily accessible at the time of the design in 2009.

Sharing space on the CDH board was the iProbe circuit to measure the plasma field around the satellite. The iProbe circuit performed a frequency sweep and measured the impedance of its probe. It communicated with the CDH processor using one of the serial ports. The iProbe circuit included a PIC18F4620 microcontroller that controlled a 180 MHZ DDS to generate a frequency-swept signal to measure the probe impedance to detect plasma density.

The other CDH serial ports were connected to the sensor board, the radio board, and the high-voltage board. The GPS receiver, the sensor board, the high-voltage board, and the radio board all were connected to the CDH board. Battery power was routed from the EPS board through the CDH board to the radio and high-voltage boards.

The debugging/programming port is located next to the microSD card and is accessible through the ARM solar panel. It is a serial port dedicated for programming and includes a boot signal used to put the microcontroller into program upload mode. The microcontroller internal FLASH memory contained the flight software. Updates were not possible after launch.

4.5 Sensor Board

The sensor board, seen in Fig. 27, had an ATMEGA168 AVR microcontroller that interfaced with all the sensors. The sensor board included a three-axis magnetometer connected though an SPI port and a three-axis accelerometer connected via I2C interface. The magnetometer was from Motorola and used magneto-resistive sensors. The accelerometer was a Bosch BMA180.

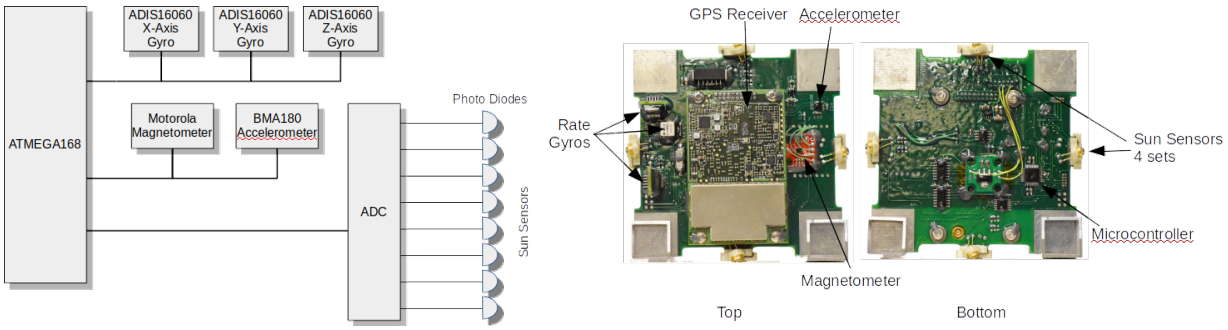

(a) Sensor board diagram

(b) Sensor board

Fig. 27—Sensor board layout

The sensor board included three gyro rate MEMS sensors (ADIS16060) mounted to provide three-axis measurements and the needed sensitivity. The components were selected before quality three-axis gyro ICs were available that had the needed sensitivity. The interface to the gyros was a unique serial interface that required the processor to bit-bang the signals via software.

Sun sensors also were included. There were eight sun sensors, with two per side, made up of photodiodes. On each side, the photodiodes were pointed at angles from each other so the angle to the sun could be determined by the ratio of the two photodiodes. All the photodiodes were measured using a simple resistor

divider circuit into an eight-channel analog-to-digital converter (ADC). With the expected intensity of the sunlight, amplifiers were not needed for the photodiodes. They operated over the full range of the ADC.

The operation of the sensor board was simple. When turned on, it waited for a command to start streaming sensor data to the CDH. The streaming rate could be adjusted, as could the accelerometer sensitivity range.

A GPS receiver was mounted on the sensor board but did not interact with the sensor processor. The GPS receiver was a Novatel receiver with software updated to support orbital dynamics. It communicated with the CDH through a serial port. The GPS antenna is mounted on the exposed z-axis panel.

4.6 Radio Board

The radio board, seen in Fig. 28, included an ATMEGA328 AVR microcontroller that handled the interface to the radio. The radio board included a half-duplex GMSK radio module, a low noise amplifier (LNA) module, and a power amplifier. The transmit and receive antennas also were connected directly to the radio board. The antennas were made of nitinol wire.

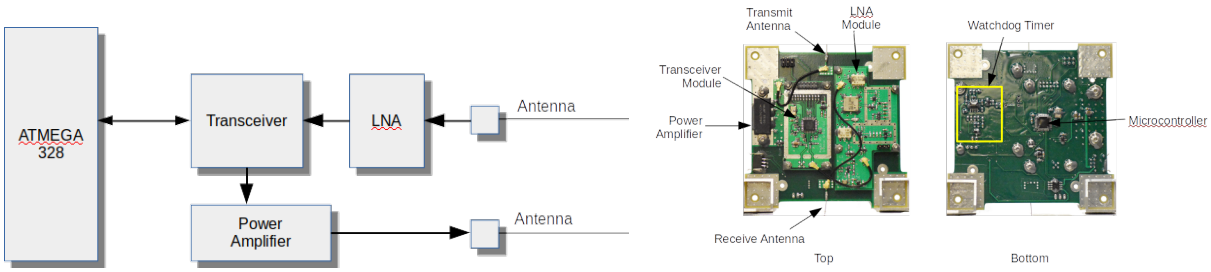

(a) Radio board diagram (b) Radio board

Fig. 28—Radio system

An Analog Devices ADF7020-1 transceiver was used. It was a half-duplex module supporting GMSK modulation. It was configured to support a 9600-bits-per-second data rate and to be compatible with the amateur radio 9600 baud waveform, which was a raised cosine FM modulation that was compatible with GMSK. The transceiver was its own module that was mounted on the radio board. The transceiver RF ports connected to the LNA and power amplifier with u.fl terminated RF cables. The transceiver performed data bit recovery and sent a clock signal and a data signal to the microcontroller when receiving. When transmitting, the microcontroller provided the data bit stream synchronized to the 9600 Hz data clock provided by the transceiver.

The LNA was a separate module that mounted on the radio board. The LNA module included amplifiers, a limiter at the input, and a mixer to shift the received signal from 297.7 MHz to 257.7 MHz because the transceiver VCO could not switch between 297.7 MHz and 253 MHz; the receive signal needed to be shifted closer to the transmit frequency to be within the VCO tuning range. The down-converted signal was selected based on in stock crystal oscillators for the down-converter local oscillator.

The power amplifier was a Mitsubishi RF power module capable of generating about 4 watts of RF based on the voltage of the satellite battery. The battery was connected to the RF power module and the output power varied based on the battery state. Anywhere from 1 watt to 4 watts was available.

The microcontroller decoded the bit stream from the transceiver and processed the AX.25 protocol data packet. Data packets contained up to 256 bytes. If the packet CRC matched, the microcontroller sent the packet contents to the CDH. When the CDH sent data for transmission, the radio microcontroller assembled the data into an AX.25 packet and sent the bit stream to the transceiver. The bit stream was scrambled to keep the bits randomized so the demodulation would work properly.

4.7 High-Voltage Board

The high-voltage board, seen in Fig. 29, established the routing of the high voltage to the tether and the collector tape and measured current through the tether and any voltage biases. The board had an ATMEGA128 AVR microcontroller and communicated with the CDH through a serial port. The high-voltage board included two high-voltage modules that could generate 150 and 300 volts each and could be combined for a maximum of 450 volts. The high-voltage output could be regulated or unregulated. The high-voltage modules had isolated outputs and a large portion of the control circuitry and the voltage- and current-measurement circuitry were also electrically isolated from the satellite bus.

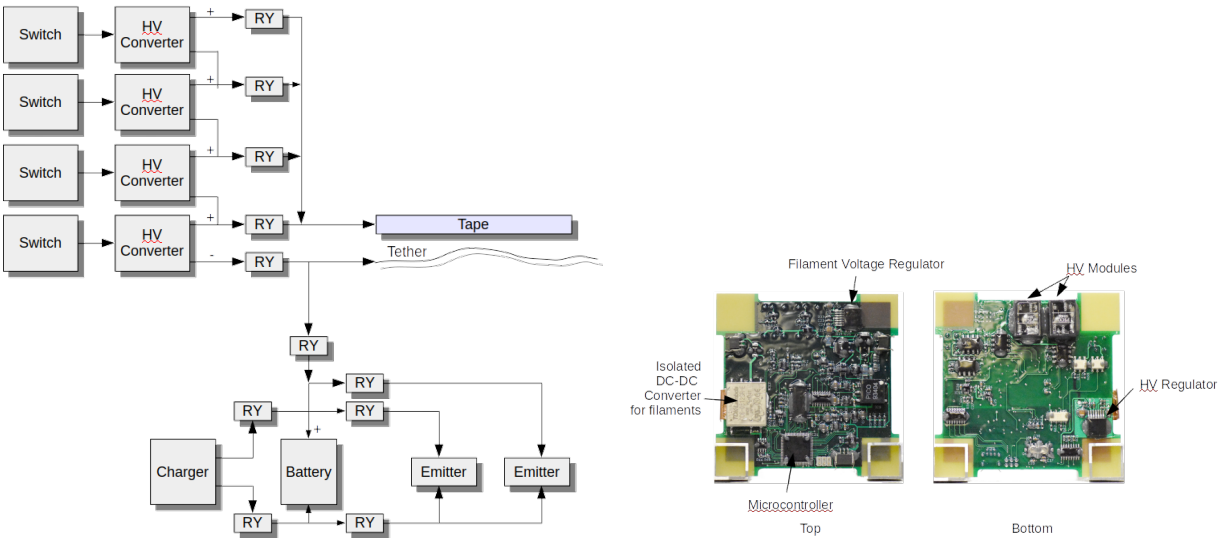

(a) High voltage diagram

(b) High voltage board

Fig. 29—High voltage

The microcontroller received commands from the CDH to open and close switches that route the high voltage to the tether or filaments and route signals for measurement. The board includes the filament drive circuitry and also was electrically isolated from the satellite bus.

Current measured through the tether was limited to 10 ma. A current-limiter circuit prevented higher currents that could damage some of the circuits.

4.8 Flight Software

The flight software used FREE RTOS as the real-time operating system. This allowed multiple tasks to operate simultaneously. The software architecture takes advantage of the RTOS by splitting critical operations into two tasks. One task is called the monitor task. It collects analog voltage telemetry and

monitors the battery voltage. If the battery voltage drops below 6.15 volts, the monitor task will shut down any science task and the attitude control task if it is running.

The second task is the command interface task. It monitors the radio board for any incoming command packets. When a command packet is received, the command interface task processes it and executes the command. The command interface task also resets the watchdog timer. The command interface task is considered the most critical task, which is why it is the only task to reset the watchdog timer. A second timer is used to determine whether a command has been received within 24 hours. If the satellite is not commanded within 24 hours, the command interface task will stop resetting the watchdog timer to force a complete satellite power cycle.

Before any tasks are started, the CDH executes a boot sequence. The boot sequence uses the EEPROM to store boot states. At first boot, the boot sequence starts a 30-minute countdown. This allows the satellite to drift a safe distance from the launch vehicle after deployment. After 30 minutes have expired, the sequence sets a byte in the EEPROM used to skip the countdown in future boots. The next step in the boot sequence is to deploy the receiver antenna by turning on the resistor cutter for 10 seconds, then turning on the second resistor cutter for 10 seconds to release the transmitter antenna. The boot code checks a byte in the EEPROM to determine whether the antenna deployment is to be bypassed. A command to the satellite is required to bypass the antenna-deployment sequence. Finally, the boot sequence starts the monitor task and the command interface task.

All other tasks are started from the command interface task, such as the attitude-control task and the script-processing task.

The attitude control task collects the sensor data and saves it to the SD card. For attitude control, all of the sensors except for the accelerometer are saved, since the accelerometer does not provide any useful data. The attitude-control task has three operating modes. One is monitoring the attitude of the vehicle and recording to the SD card. The second mode is active attitude control operating the magnetorquer coils. The third mode is determining when the satellite is within 20 degrees of NADIR and triggering the tether release. The task and modes can be turned on and off at any time by command.

The script-processing task receives a script to operate the GPS receiver and high-voltage board at specific times with a 1-second resolution. The script will call each operation as a function. For GPS operations, the script will call the GPS receiver function, which will turn on the GPS receiver and will monitor for valid data. Once the GPS receiver gets a valid time, the function will record the X, Y, and Z position generated by the receiver. The function operates for a specified number of seconds.

The iProbe function turns on the iProbe circuitry and sends a series of bytes that configure its operation. Within a second, the iProbe returns about 3 kilobytes of data that is stored in the SD card and is turned off.

For the high-voltage board, there are several functions that perform different operations, including filament carburization, emission testing, measuring the electromagnetic field, and thrusting. The script-processing task executes the selected function at the specified time. Even though the flight software is identical, the flight software is compiled with a flag set to indicate if the end mass is Ren or Stimpy. This distinction will determine how the function operates. This allows the same exact script to be sent to both end-masses. For example, in the thrusting operation, when the function is configured to emit, Ren will be the emitter and Stimpy will become the collector. The code inverts the operation based on the identity compiled.

The script-processing task allows for multiple operations to be performed in sequence. Due to limited power availability, only one operation can be performed at a time. Powering on the GPS receiver, the iProbe circuit, and the high-voltage board simultaneously would overload the battery. Multiple simultaneous access to the SD card is also problematic.

Download operations are performed as a function called from the command interface task. A file from the SD card can be selected for download either by requesting the whole file or requesting a range of blocks from the file. Block sizes are 252 bytes. Downloading blocks allows the ground station to determine whether any blocks were not received and those blocks can be requested again. When a series of blocks is requested, it is downloaded in sequence. There is no handshaking performed for each block download. That potentially would increase the length of the download process. Many of the data files were formatted so that missing blocks would not make the data unusable. The GPS data formatted into binary, four-byte words, and each packet contained a complete set of data including time tags. Missing packets would not prevent the downloaded blocks from being used. The sensor data was configured the same way. The high-voltage data was written in ASCII format, and recovery from missing blocks was simple.

4.9 ACS Algorithm and Software

4.9.1 Tether Deployment

The attitude control system was designed to maintain nearly in-plane rotation of the spacecraft at a rate of 1 rpm prior to deployment to provide favorable deployment opportunities every half-minute. Once authorized from the ground, one of those opportunities would be used to cut the stacer tie-downs and to start deployment. Because spacecraft resets were becoming more frequent, it was decided to issue a manual deployment command.

Sensor data was captured during deployment and was downloaded. It showed a very clear dynamic signature of the stacer action. Before deployment, Ren was rotating about the x-axis normal to the long axis of the spacecraft at a rate of 14 deg/s. The other two components of the angular velocity were relatively small. Within a second after stacer release, spacecraft rotation about the x-axis practically stopped because the moment of inertia increased drastically, and Ren was spun up to 95 deg/s about the axis of the stacer (z-axis) because of the unwinding of the stacer string, as shown in Fig. 30. This happened exactly how it was observed in the early drop tests in the lab, indicating that the stacer deployment was nominal.

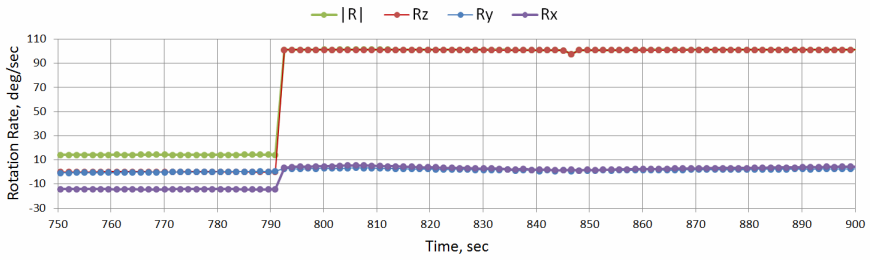

Fig. 30—Stacer deployment signature in the rate gyro data

Many deployment simulations were conducted during the design phase. They all indicated that a bounce at the end of deployment was inevitable. When the deployment direction was relatively close to the local

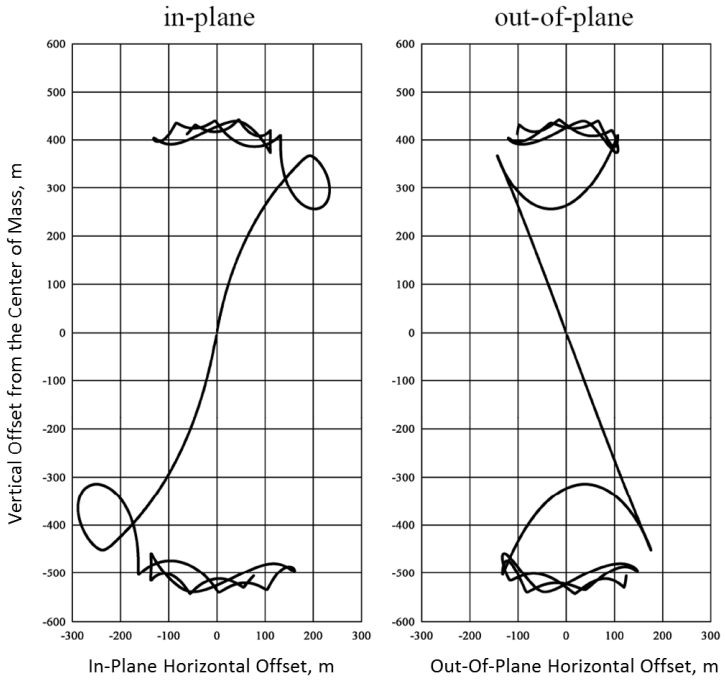

Fig. 31—Tether deployment simulation

vertical, the bounce was smaller, as shown in Fig. 31, while in other cases, it was larger. Consequent bounces also were common.

To reduce the end-of-deployment bounces, copper wire hooks were embedded in the tether winding along the last segment of the tether. When the tether pulled on a hook, as shown in Fig. 15b, the wire was straightened and the energy was dissipated in a relatively consistent way, reducing the magnitude of the next bounce. This caused the bouncing to stop in a few orbits as the system transitioned to libration.

While there was no data to gauge the number and the magnitude of the post-deployment bounces, it is known that after deployment, the system settled into libration, with a moderate amplitude on the order of 20 deg both in plane and out of plane.

4.9.2 Collector Tape Deployment

Collector tape deployment was commanded on 11/22/19. Deployment success was confirmed by analyzing the ACS data downloaded over the next days.

Figure 32 charts magnetometer and rate gyro data downloaded from Ren on 11/28/19. Ren's attitude motion shows signatures of slow oscillations with a period around 6 min and fast oscillations with a period around 3.5 s. Both are somewhat irregular. The slow component is consistent with pendular oscillations of the end-body with appendages (the collector tape and the stacer) driven by the torque of the low tension force of the attached tether. The fast component is consistent with the first mode of bending oscillations of the fully deployed collector tape.

According to this data, Ren's z-axis must have been closely aligned with the tether, and there was a very strong coupling between its attitude motion and bending oscillations of the collector tape. It is

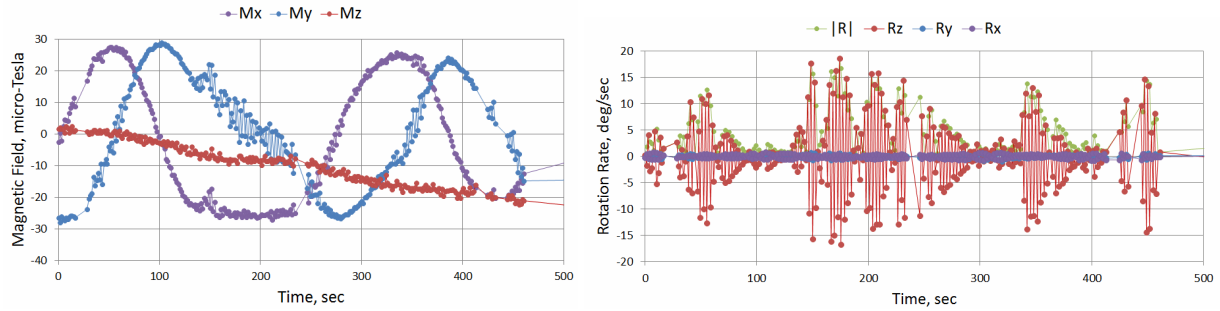

(a) Collector tape oscillation signature in the ACS data

(b) Collector tape oscillation signature in the ACS data

Fig. 32—Tape oscillation signature in the ACS data

understandable, since the moment of inertia of the 5 m collector tape was much larger than Ren's moment of inertia, and even small deflections of the collector tape caused large disturbances in Ren's rotation. It is interesting to note that these coupled oscillations did not subside and must have been feeding off the energy of libration and tether oscillations.

4.9.3 Tether Libration

Assuming that the long axes of the end-bodies were closely aligned with the tether line, it was possible to estimate tether angles to the local vertical on certain subsets of the ACS data. These solutions are plotted in Fig. 33. The average in-plane angle was 12 deg, while the average out-of-plane angle was 10 deg. The maximum angles (libration amplitudes) were about 23 and 20 deg, respectively.

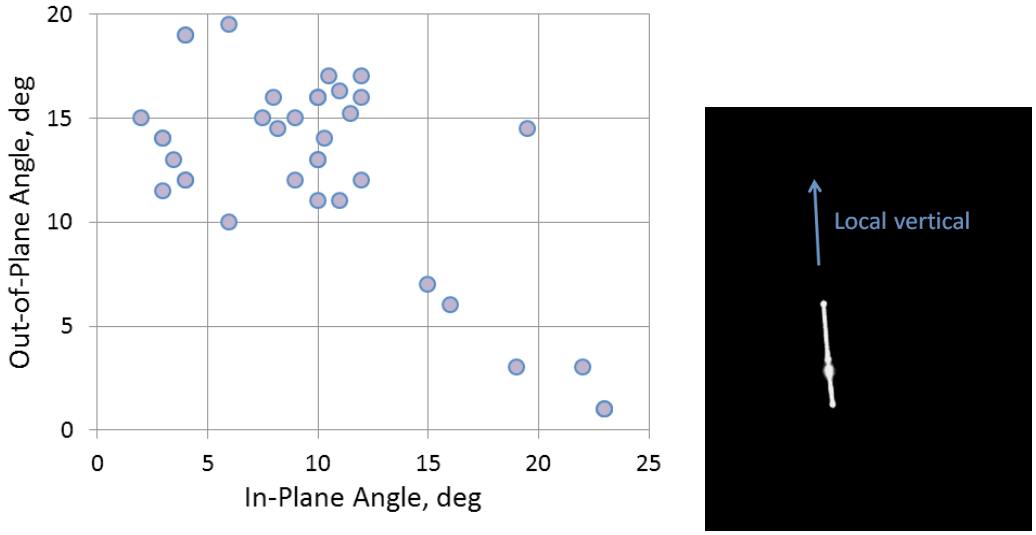

(a) Estimated libration angles

(b) TEPCE imaged from Chile by PlaneWave

Fig. 33—Tether libration

The fact that the tether remained relatively close to the local vertical was confirmed independently by the analysis of the series of TEPCE images obtained by Matt Dieterich of PlaneWave Instruments on 12/5/19 and 12/7/19 from El Sauce Observatory in Chile.

4.9.4 Attitude Motion Before Deployment

After ejection from the CubeSat dispenser, TEPCE was found in nearly pure single-axis rotation about the x-axis and remained in this state for the entire pre-deployment period. Figure 34 shows a typical block of rate gyro data downloaded from Ren on 8/3/19.

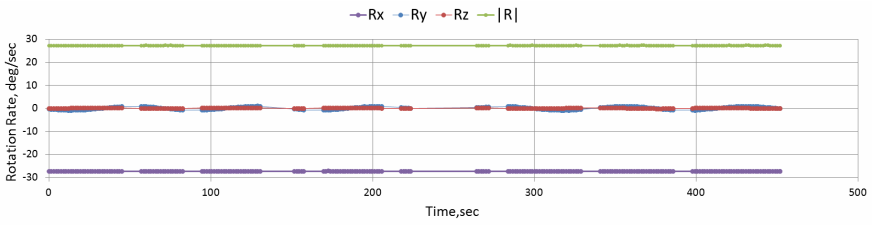

Fig. 34—Pre-deployment rotation state

Data processing during the pre-deployment period included 42 rotation state assessments covering all available ACS data and three ACS recalibrations, in July, October, and November of 2019. The following effects have been observed and quantified:

- Short-term precession of the angular velocity vector due to a small difference between the moments of inertia Jx and Jy; it has been estimated that Jx was larger than Jy by 6%;
- Long-term precession of the angular momentum vector due to residual magnetization; the residual magnetic dipole has been estimated to be around 0.005Am^2;
- Rotation rate drift due to the magnetic torque from currents in the solar panels; a characteristic magnetic dipole produced by these currents has been estimated to be around 0.0002Am^2.

The rotation history had four distinct periods illustrated in Fig. 35:

1. A downward drift due to the magnetic torque from solar panel currents,
2. Active detumbling by the AC,
3. An upward drift due to the magnetic torque from solar panel currents, and
4. Active detumbling before deployment.

4.9.5 Attitude Control System

Both Ren and Stimpy had identical sensor boards and were running identical attitude determination and control software. Each sensor board had a Freescale Xtrinsic MAG3110 magnetometer, three Analog Devices ADIS16060 gyroscopes, a Bosch BMA180 accelerometer, and eight Panasonic PNZ331CL photodiodes. The spacecraft coordinate system and the sensor board layout are shown in Figs. 27 and 25b.

Each of the end-bodies had two identical magnetorquer coils. Ren had coils on the -X and Y faces, and Stimpy had coils on the -X and -Y faces. Ren's Y-face coil is shown in Fig. 25b.

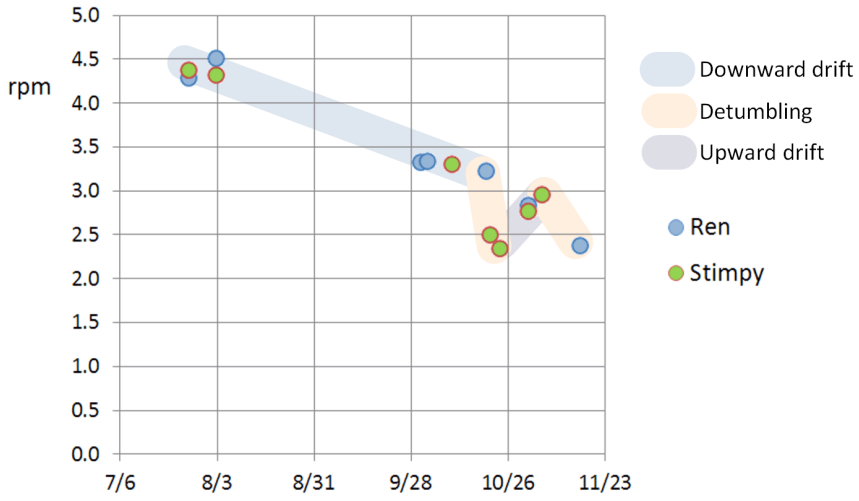

Fig. 35—TEPCE rotation rate evolution

A special control law called "Modified B-dot" was developed to bring the spacecraft into slow rotation about the normal to the orbital plane in order to provide favorable deployment opportunities every half-minute or so. It adds a target rotation rate to the well-known B-dot control as follows:

$$\boldsymbol{m_c} = k(\boldsymbol{\Omega} - \Omega_0 \boldsymbol{e_n}) \times \boldsymbol{B},$$

where $\boldsymbol{m_c}$ is the control torque, k is a coefficient, $\boldsymbol{\Omega}$ is the angular rate vector, Ω_0 is the desired rotation rate, $\boldsymbol{e_n}$ is the vector normal to the orbital plane, and B is the geomagnetic field vector.

The rotational state of the spacecraft was determined by processing magnetometer, sun sensor, and rate gyro data. The processing was based on a theory of short-arc solutions developed specifically for TEPCE. One of the requirements was that it should work both in pre-deployment and post-deployment phases, even though they were completely different dynamically.

The attitude determination algorithms and software were tested and calibrated on a two-axis turntable built for this purpose.

The ACS software was designed to be configurable in flight by changing and uploading any of its 33 parameters. This allowed recalibration of the ACS system in orbit, accounting for the changes in the system configuration, residual magnetization, and other factors.

5. FLIGHT OPERATIONS

The TEPCE ground system consisted of a remote ground station (RGS) at a Naval Research Laboratory installation at the Naval Air Station Trumbo Point, Key West, FL. The RGS was controlled by the TEPCE Mission Operations Center (TMOC) at the Naval Research Laboratory in Washington, D.C. The Key West location was chosen due to the accessibility of NRL property and a computer network on the site and the high-elevation, low-range passes that occur over Key West for the TEPCE orbit due to the low inclination of

the orbit. A link budget analysis performed by engineers at NRL found that the transmit power of TEPCE was insufficient to secure downlink to a ground station located in Washington, D.C. Average bandwidth between TMOC and RGS was about 22 Mbps, which was sufficient for TEPCE state of health monitoring, commanding, and data transfer. Figure 36 gives an illustration on the TEPCE ground architecture.

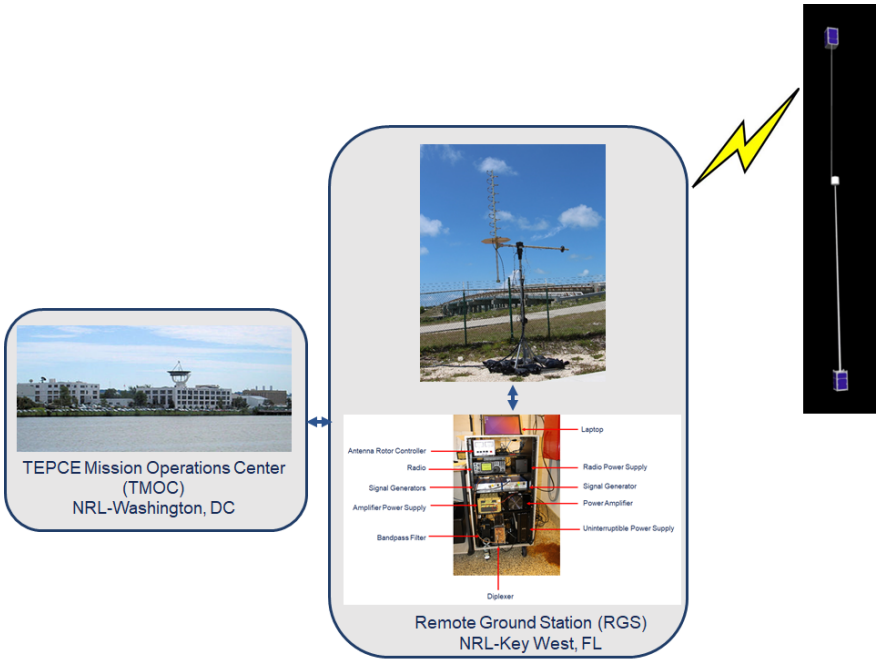

Fig. 36—TEPCE ground architecture

The RGS consisted of an M2 Antenna Systems Inc. 2.4-m helical antenna attached to a 10-foot-tall antenna mount with a YAESU G-5500 antenna azimuth-elevation rotators & controller. The motor was controlled via a custom rotator controller connected to the on-site laptop.

The on-site laptop provided azimuth and elevation input based upon a custom-built tracker program that received input from an open-source satellite position tracking program called PREDICT[5]. Screenshots of the PREDICT program are shown in Figs. 37a – 37c. A custom motor controller and tracking program was built utilizing the PREDICT data, which allowed for automated control of the azimuth and elevation motor, shown in Fig. 37d. A custom-built satellite control program was developed to generate transmission signals and to process received data. Figure 37e shows the TEPCE graphical user interface used during operations.

The TMOC computer was used to receive remote video of the ground station via a webcam as well as to update and control the RGS computer via the Remmina remote desktop program available in the Ubuntu 16.04 LTS distribution of the LINUX operating system utilized by both computers.

5.1 Launch and Deployment of Tether

TEPCE was launched from Cape Canaveral, FL, on June 25, 2019, on Space Test Program (STP-2) mission SpaceX Falcon Heavy. TEPCE was stored inside of a Poly Picosatellite Orbital Deployer (PPOD) mounted to the payload attachment fitting of the upper stage. TEPCE was deployed from the PPOD approximately 19 minutes after liftoff.

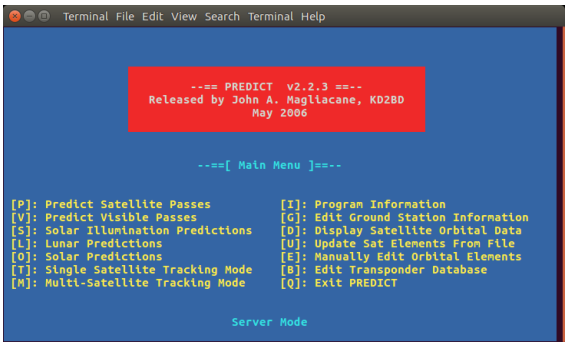

(a) PREDICT software used for TEPCE tracking

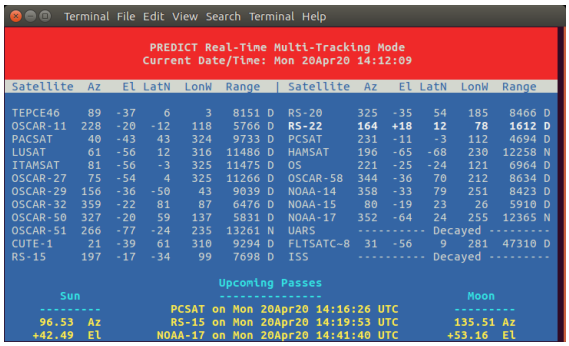

(b) PREDICT software multi-tracking mode

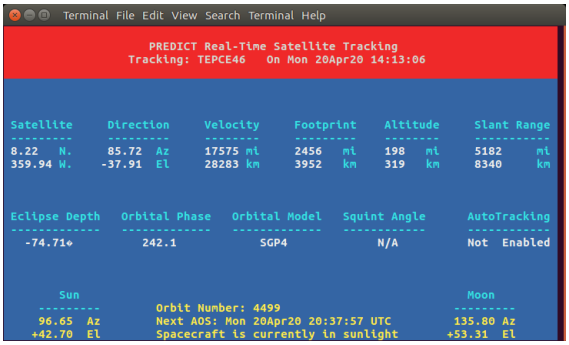

(c) PREDICT software single-tracking mode

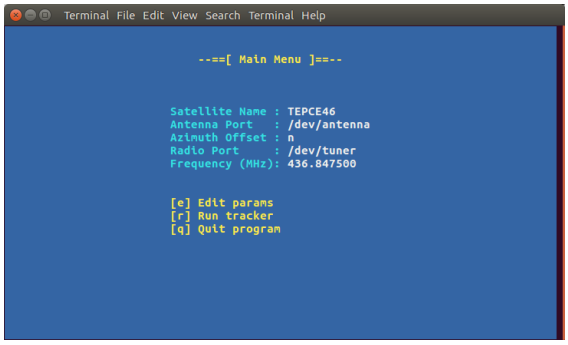

(d) Custom-built motor controller/tracking software

(e) TEPCE GUI — controlling Stimpy

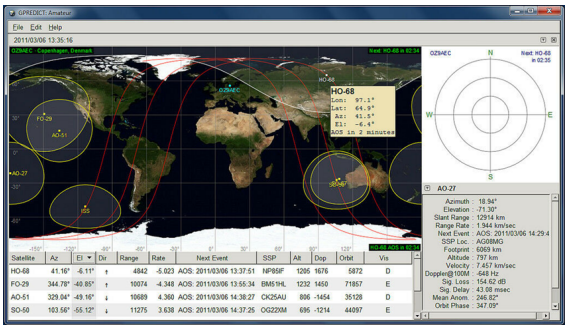

(f) PREDICT software used for tracking the path of TEPCE

Fig. 37—Control software images

TEPCE was one of several CubeSats launched as part of the STP-2 mission. This attributed to a delay in identification, as the two weeks after launch were spent trying to positively identify TEPCE from the list of TLEs published to Space-Track.org [6] via a system of trial and error. This process involved tracking each TLE during passes over the RGS, sending "Find State" commands, and awaiting a response from TEPCE. In order to slightly automate the process and maximize the chance of making successful contact, a program was built based off of the existing satellite control software to send a signal to each end-mass in alternating, 3-second bursts. The signal consisted of a command to increase transmitter power to maximum and to return state telemetry. The team noticed that while tracking satellite number 44346, both the automated pinger and the original control software would encounter errors. Upon review of the code, it was determined that an error in the ground station software was mishandling positive signals from TEPCE. The errant parts of the code were corrected and positive contact was made to satellite number 44346 on July 16, 2019, confirming that it was, in fact, TEPCE. Since TEPCE consisted of two independent end-masses, contact first was made only with the Ren end-mass. The Stimpy end-mass was not able to establish communication until July 22, 2019.

5.2 Subsystem Checkout

Following the successful contact with TEPCE, a series of system checks were initiated. These checks included synchronization of onboard clocks, activation of attitude control systems, activation of GPS receivers, download of telemetry and sensor data, and upload of configuration files. Upon review of gyroscope data, it was determined that TEPCE was tumbling end over end at a rate of 4.4 revolutions per minute about the spacecraft‘s x-axis. This was far above the maximum rate acceptable for tether deployment of one RPM, resulting in the need to engage the onboard torque coils to slow the tumbling.

TEPCE’s orbit encountered the South Atlantic Anomaly and because the onboard electronic components were not radiation-tolerant, several resets occurred. Mining of this flight data is available to any group that would like to correlate the TEPCE orbit with the onboard resets in order to validate South Atlantic Anomaly models.

On the morning of November 16, 2019, at approximately 0140 EST, the command was given to deploy the tether, separating the two end-masses. Acknowledgement of successful deployment was not obtained; however, subsequent passes showed an increase in the rotation rate about the roll axis that was consistent with the rate of the stacer unwinding per prelaunch tests. A sixfold increase to the drag term on November 17, 2019, further confirmed separation of the spacecraft. On November 22, 2019, commands were given to deploy the impedance probes (iProbes) and collector tapes for both end-masses. Confirmation was received from Ren; however, due to communication limitation with Stimpy, confirmation of iProbe and collector tape deployment could not be determined. Imagery on November 21, 2019, further confirmed separation of the end-masses but showed separation of only about 270 m. Further imagery on November 27, 2019, showed a separation of 450 m but also an anomalous reflective area in the center of the tether. It is suspected that a snag in the tether prevented full deployment. Possible causes may be due to periodic reversals of the winding direction of the tether around the spacer, a snag of a piece of hardware, or a memory effect within the tether.

A timeline of the major milestones in the TEPCE mission, from launch to reentry, is shown in Fig. 38.

5.3 Communication Lessons Learned

TEPCE suffered from varying communication problems throughout the mission. Issues included communication difficulties between the TMOC and the RGS computer systems, difficulties closing the link with

Milestone	Event Date
Falcon Heavy Launch of TEPCE	6/25/2019
Initial Contact with Vehicle	7/17/2019
Initial ACS Sensor Data Collection	7/22/2019
Initial GPS Data Collection	8/19/2019
Torque Coil Activation	10/22/2019
TEPCE Tether Deployment	11/16/2019
Collector Tape Deployment & Filament Carburization	11/22/2019
Impedance Probe Deployment	11/23/2019
Impedance Probe Data Collection	11/25/2019
Thrust Commanding Returned Current Readings	12/5/2019
TEPCE Re-Entry	2/1/2020

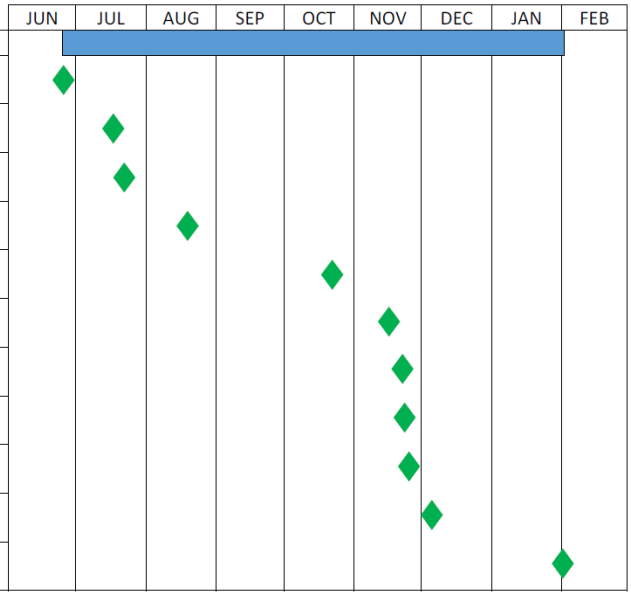

Fig. 38—TEPCE mission timeline with major milestones

the satellite, tracking issues with the ground station, and power management issues with the end-masses. The spacecraft was started some 10 years before flight, and for various reasons had to wait a significant amount of time for launch. Thus, many parts used in TEPCE were not as modern as they might have been. For budgetary reasons, it was not possible to change components late in the development of TEPCE.

Prior to launch, communication checks were performed between the TMOC and the RGS. Due to the fact that this mission was a part of a Department of Defense research program, both the TMOC and the RGS communicated over a DoD telecommunications network, managed by the Naval Research Laboratory in Washington, D.C. The semi-remote nature of the ground station site in Key West meant that internet connectivity required a microwave transmitter back to a centralized building at NAS Key West, which then established a connection to NRL DC via a virtual private network (VPN) connection. These layers of communication resulted in significant delay and communication lag in the testing period prior to launch. Lag of up to 25 seconds was common when utilizing the remote desktop control as well as dropped communication between the networks. Staff at NRL Key West made significant improvements by adjusting the microwave transmitter to increase both the reliability and the bandwidth to the ground station site. This resulted in next-to-no network drops and a 2-second lag, which was acceptable for operations.

During the pre-tether deployment phase, the rotational motion of TEPCE and null patterns in the antennas increased the difficulty of closing the downlink. The TEPCE operations team experienced sporadic loss of communications with one end-mass or the other for short periods of time. Reduction of the satellite's spin rate helped to increase the connection times that allowed for downloading of more data from each end-mass, execution of more commands per pass, and the uploading of larger multiprocess scripts. Due to the directionality of the monopole antennas used for transmit and receive on each end-mass, orientation of the spacecraft directly affected the ability to communicate with the spacecraft. There were also orientations for which an end-mass was able to receive commands; however, the transmit antenna was not pointed toward the Earth, so confirmation could not be made. Additional antennas in different orientations on future spacecraft would help reduce a lack of communication due to orientation. Also, a system of relaying signals between

two different end-masses would allow one end-mass to pass commands through in the event that the target end-mass is in a null orientation to the ground station.

The ground station initially encountered issues with northern satellite passes that traveled through the 000 azimuth. The default setting for the motor would cause the antenna motor to stop at azimuth 359 and to rotate in the opposite direction of travel, and then to return to normal tracking after returning to a 000 azimuth position. This was a safety feature to prevent cabling from wrapping around the antenna mast; however, the slew rate of the motor meant that up to a minute of contact time was lost when the motor reset itself. A simple software setting was adjusted, allowing the motor to rotate an additional 90 degrees before returning to the 000 position, which eliminated the issues during northern passes.

Closing the downlink with Stimpy became very difficult during the post-tether-deployment phase of the mission. After deployment, the gravity gradient caused the Stimpy end-mass to remain at a higher altitude compared to Ren. It is hypothesized that the tether may have modified the antenna pattern, causing a null in the direction of the antenna. A few sporadic contacts with Stimpy were made, but it could not be determined what factors, if any, allowed for these seemingly random contacts. The operations team made 1,230 communication links with Ren, whereas only 41 links were made with Stimpy.

Contact was made more often with the bottom end-mass, Ren, than the top end-mass, Stimpy, due to better communications with Ren. Stimpy had one contact post-tether deployment on November 17th and no contacts until January 2nd. After that, the majority of Stimpy contacts occurred, but none was sustainable for any type of payload operation. A relay system between the end-masses, as described previously, may have been able to increase contact with the higher-altitude end-mass. However, due to many CubeSat constraints, these options were not feasible.

Toward the end of the mission, weather conditions in Key West caused alignment issues with the ground station. Following a heavy storm, the azimuth and elevation of the antenna became misaligned. Fortunately, on-site personnel at NAS Key West were able to make adjustments as directed by the TEPCE team, who were able to observe via the webcam. Following these adjustments, it was determined that the motor was starting to drift from initial calibration. Since recalibration of the motor was not viable due to the remaining operational window and project funding, azimuth and elevation offsets were added to the tracking program to allow for manual adjustment.

In the final days of the mission, the onboard batteries of Ren began losing their ability to hold charge and possible electrical latch-ups caused near-constant current draws on the batteries. This prevented Ren from completing scripted operations, as the batteries would drain below a usable level prior to completing the sequence of operations. As the situation got worse, the maximum voltage of the batteries began dropping to a level that a single "FIND STATE" telemetry command would drain the batteries to a level that triggered an automatic restart. Since Ren was the only end-mass that could be contacted reliably during the mission, all high-voltage operations, data collection, and communications were done via Ren vice being distributed between the end masses. The inability to communicate with Stimpy likely accelerated the degradation of the batteries. Additionally, the length of the pre-deployment phase likely attributed to degradation, as subsystem checkout continued longer than initially budgeted.

5.4 Orbital Lifetime

Engineers on the TEPCE team performed a post-tether deployment orbital lifetime analysis of TEPCE prior to launch as part of the orbital debris requirements. The purpose of this analysis was to create bounds on

the expected orbital lifetime of TEPCE after tether deployment, given that the primary science experiments could occur only after tether deployment. The gravity gradient between the two end-masses caused a libration motion in the dynamics, so the area-to-mass ratio of the spacecraft was not constant. The lifetime bounds were generated by selecting upper and lower bounds of area-to-mass ratio and propagating the orbit state with those two area-to-mass ratios using the STK HPOP propagator with an NRLMSISE2000 [7] atmosphere model and an EGM2008 [8] geopotential model. The upper bound of area-to-mass ratio corresponded to the lower bound in area-to-mass orbital lifetime. Likewise, the lower bound in area-to-mass ratio corresponded to the upper bound in orbital lifetime. The upper bound in area-to-mass ratio was computed by assuming no librational motion and using the maximum cross-sectional area of the deployed tether and both end-masses divided by the measured mass of TEPCE. The lower bound in area-to-mass ratio was taken as the cross-sectional area for a libration angle of 45 degrees.

The above analysis predicted a post-tether deployment orbital lifetime between 30 and 60 days. TEPCE reentered Earth‘s atmosphere on February 1, 2020, resulting in a post-tether deployment lifetime of 78 days. This longer-than-expected lifetime is attributed to a partial deployment of the tether and therefore a smaller area-to-mass ratio than expected. This hypothesis was backed by imagery collected by the AMOS 1.6 m telescope. The image showed significant glints in the middle of the tether, indicating bunches in the tether. Note that passive electrodynamic drag was not taken into account in the analysis.

Once the two end-masses were separated, it was a race against time to conduct as many electrodynamic experiments as possible. Approximately two weeks after separation from SpaceX, Space-track.org began posting element sets for TEPCE. The official element set number was 44346.

The end-masses were separated on November 15, 2019. The exposed tether increased the area for TEPCE, which resulted in a significant increase in the decay rate. The last element set published was on February 2, 2020, which was 78 days after separation of the end-masses. As seen in Fig. 39, the last few element sets exhibited marked increase in decay. The date of the last element set provided by Space-track.org was February 2, 2020, which indicated that was the date TEPCE reentered the atmosphere. The enormous drag produced by the tether shortened the life of TEPCE by some 6 years. It is well known that electrodynamics can further decelerate the orbit of a tethered satellite. Many papers have been published on the deceleration effects of electrodynamics thrusting, [9].

5.5 End-Mass Deployment

From their 1.6 m telescope, the Air Force Maui Optical & Supercomputing (AMOS) site provided an image, Fig. 40, of TEPCE after separation of the end-masses. The image showed a significant bunching in several places along the tether. It was estimated that the separation between the end-masses was approximately 400 m, not the full 1 km. One theory was that the tether got tangled upon deployment even though energetic spring-forced deployment was designed to eliminate possible tangling. Another possibility was that gravity gradient forces were insufficient to overcome the memory in the tether. The tether was wrapped in its stowed condition for some 7 years. Gravity gradient forces were expected to overcome the shape memory in the tether.

TEPCE‘s visible length is apparently 400 m - 500 m, much less than the 1030 m of full deployable length. The bright spots along the tether did not move during the pass, so they are not caused by glint. They seem to be tether snags created after a rebound. This suggests that the wire braking hooks deployed too easily,

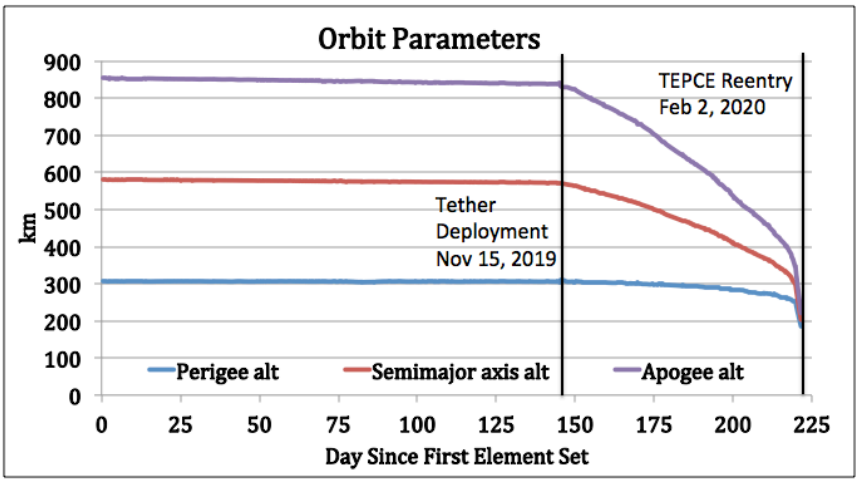

Fig. 39—TEPCE orbit parameters

so they did not slow down deployment much. Or perhaps one was too strong, and stopped the deployment suddenly. In either case, there was enough energy at the end of deployment to cause a large rebound.

The wound tether was stored for 7.7 years before deployment. Other stored tether samples have a springy set that may allow weak snags, somewhat like those often found in long, helical telephone cords. Tether deployment took only about 4 minutes. Fast deployment causes an in-plane libration greater than 35 degrees. But TEPCE appeared to be closer to vertical than that. Pulling out the weakest parts of snags may have damped TEPCE's libration far faster than occurred with the 4 km TiPS tether, which deployed in 1996.

Fig. 40—Image of TEPCE after tether deployment taken at the Air Force Maui Optical and Supercomputing (AMOS) site

6. THRUSTING AND CURRENT FLOW RESULTS

The communications and battery-life issues discussed in previous sections severely limited electrodynamic tether operations once TEPCE's tether was deployed. Nonetheless, TEPCE was able to return some interesting physical measurements. Since Stimpy was basically nonoperational after tether deployment, tests in which a bias voltage was to have been applied to its collector tape could not be conducted; in fact, the collector tape was never made part of the electrodynamic circuit. This situation was mitigated in part, first by the fact that the tether, itself, was conducting, and second by the fact that Ren, as the lower-altitude end-mass, was on the negative end of the tether, so that by simply igniting its electron-emitting filament, current could be made to flow in the electrodynamic circuit, driven by the naturally occurring potential drop in the tether.

Ren's electron-emitting filament could be heated to various levels, but only the lowest level of heating was necessary for successfully closing the electrodynamic circuit. The scheme for data collection from Ren's current meter was fixed at 2-second intervals, and the data bandwidth was such that a maximum of approximately an hour's worth of current data could be collected and transmitted per day of operation. Unfortunately, this maximum was able to be achieved on only one day, Dec 6, 2019, after tether deployment; however, on that day, just shy of two complete orbits of electrodynamic tether data was collected, with approximately 33% coverage over that time span. The tether current as a function of time for this data set is shown in Fig. 41.

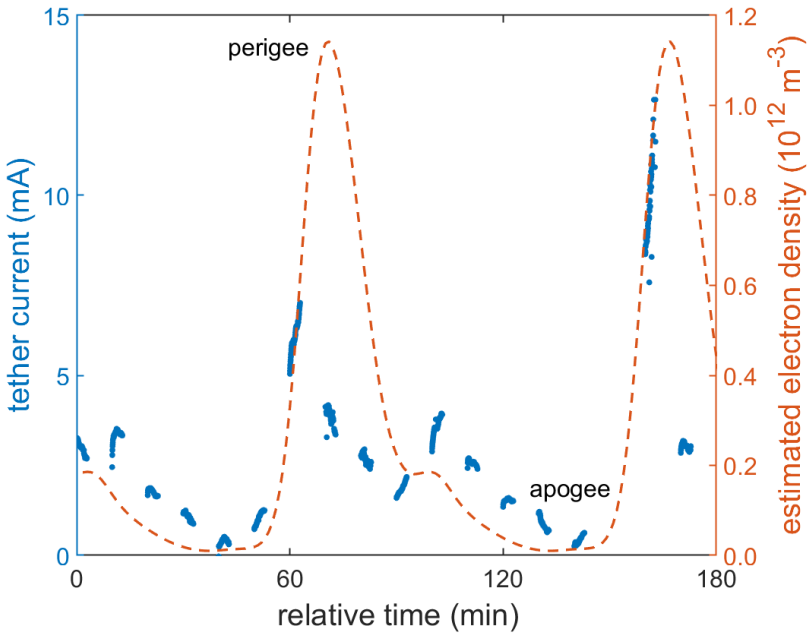

Fig. 41—Measured tether current and estimated plasma electron density over approximately two orbits, taken Dec 6, 2019.

The impedance probe (iProbe) on Ren was operational; however, the iProbe was designed to measure the ambient plasma density through resonance with the plasma electrons, and these were excluded from the vicinity of the probe by the natural negative bias of that end of the tether. Because no data was available from the iProbe on Stimpy, it was necessary to estimate the ambient electron density using the spacecraft's position

and the International Reference Ionosphere (IRI) model. Because of the eccentricity of TEPCE's orbit, one would predict that the spacecraft sampled a plasma environment that varied by more than two orders of magnitude in plasma density, and the behavior of the current in the electrodynamic circuit is consistent with this level of variation. The orbital periodicity of the data is clearly evident. Although the peaks in the collected current are narrower than the plasma density would imply, as the satellite rose toward apogee and the ambient density dropped off considerably, the collected current fell off at a slower rate, indicating that the sheath surrounding the positive end of the tether was able to expand into the thinning plasma to support the return current in the circuit.

The maximum current shown in Fig. 41 was near the saturation current for the metering circuit and its analog-to-digital converter. On subsequent days, although only snippets of current data could be downloaded, the current meter was saturated as the satellite dipped into the dense ionospheric plasma at perigee. Given that this occurred with a less-than-fully deployed tether, with no bias on the collecting element, and with the minimum heating current applied to the filament, it is promising in terms of a simple tether system's being applied as a de-orbiting element for spacecraft.

7. SUMMARY

TEPCE demonstrated the feasibility of electrodynamic propulsion. The tie-down mechanism and the stacer spring executed successfully. The shortened distance between the end-masses is an area for future research for future missions. The communication system was designed for a short-duration mission, but evidently, non-radiation-hardened components exhibited decreased performance as time went on. Data from the electrodynamics experiments demonstrated significant electron flow along the tether.

ACKNOWLEDGMENTS

We would like to thank Matt Krupa, Luke Davis and the rest of NRL Code 6136, Corrosion & Marine Engineering staff at NRL Key West, FL, for their assistance in the installation, testing and support of the TEPCE Remote Ground Station, NRL Code 8241, RF Systems, for their analysis expertise and utilization of their antenna system, Amanda Conti and others at the Air Force Maui Optical & Supercomputing site in Maui, Hawaii for the TEPCE imagery.

Over the years, there were many contributors to the TEPCE engineering, build and testing to whom we express appreciation, including, Steve Koss, Paul Oppenheimer, Adam Thurn, Jordan Schlater, Peter Hagan, Curt Hogan, Chris Compton, Aaron Hoskins, Alan Segerman, Tony Zhao, James Doggett, Seth Westfall, Chris Tiu, Tommy Summers, Yunghsin Chen, Steven Tomaszewski, Kathy Seymour, George Kirby, Wayne Simon, Tim Holman, Thuy Dao, Darrell Griffith, and Adrienne Rector.

The research and development of TEPCE were supported by the Naval Research Laboratory 6.2 funding.

REFERENCES

1. S. Coffey, J. Carroll, P. Oppenheimer, J. R. Schlater, I. Galysh, E. Levin, C. Hogan, and A. Thurn, "SEPARATION SYSTEM AND BURN WIRE RELEASE MECHANISM FOR TETHERED SPACECRAFT, United States Patent Office 2015.

2. A. Thurn, "BURN WIRE RELEASE MECHANISM FOR SPACECRAFT AND TERRESTRIAL APPLICATIONS, United States Patent Office April 2015.

3. S. Coffey, B. Kelm, W. Barnds, W. Purdy, and M. Davis, "TiPS: Results of a Tethered Satellite Experiment," Proceedings of the Advances in the Astronautical Sciences, volume 97 (American Astronautical Society, Univelt), June 1997.

4. I. Katz, J. R. Lilley, Jr., A. Greb, J. E. McCoy, J. Galofaro, and D. C. Ferguson, "Plasma turbulence enhanced current collection: Results from the plasma motor generator electrodynamic tether flight," *Journal of Geophysical Research* **100**(A2), 1687–1690 (February 1995).

5. J. A. Magliacane, "PREDICT." URL `www.qsl.net/kd2bd/predict.html`.

6. "Space-Track.org: Database of Two Line Element Sets of Space Objects." URL `space-track.org`.

7. J. M. Picone, A. E. Hedin, D. P. Drob, and A. C. Aikin, "NRLMSISE-00 empirical model of the atmosphere: Statistical comparisons and scientific issues," *Journal of Geophysical Research: Space Physics* **107**(A12) (2002).

8. N. K. Pavlis, S. A. Holmes, S. C. Kenyon, and J. K. Factor, "The development and evaluation of the Earth Gravitational Model 2008 (EGM2008)," *Journal of Geophysical Research: Solid Earth* **117** (2012).

9. J. R. Sanmartín, M. Charro, X. Chen, E. Lorenzini, G. Colombatti, D. Zanutto, J. F. Roussel, P. Sarrailh, J. D. Williams, K. Xie, E. M. Garret, F. G. de Quiros, O. Roemer, R. Rosta, T. R. Zoest, J. Lasa, and J. Marcos, "A universal system to de-orbit satellites at end of life," *The Journal of Space Technology and Science* **1**(26) (2012).